Spatio-temporal evolution of coherent vortices in wall turbulence with streamwise curvature

Mitsuhiro Nagata* and Nobuhide Kasagi

Department of Mechanical Engineering, The University of Tokyo
Hongo 7-3-1, Bunkyo-ku, Tokyo 113-8656, Japan

(Published in *J. Turbulence* **5**, 017 (2004))

Abstract

Effects of wall curvature on the turbulent structure in curved channel flow are studied by means of direct numerical simulation (DNS). Four different radii of curvature, $\delta/R_c = 0.013$, 0.05, 0.1 and 0.2, are examined. The DNS results show reduction of turbulence intensities on the convex side and enhancement of radial turbulence intensity in the center region of channel with the increase of curvature. Analyses on the flux Richardson number and the Reynolds shear stress clarify that such turbulence modulation is attributed to the extra production of the Reynolds stress caused by the centrifugal force. In addition, a spatio-temporal LSE (Linear Stochastic estimation) is applied to the computed velocity field in order to extract the development of turbulence-producing eddies affected by centrifugal force. The development of turbulence-producing motion on the convex side is associated with a large-scale strong roll-cell working against the centrifugal stabilizing effect. The spatio-temporal LSE also reveals that on the convex side strong outward and inward motions are induced by the roll-cell before the second- and fourth-quadrant motions are developed.

1 Introduction

Flow over a curved surface frequently appears in various industrial applications such as aerofoils, turbine cascades and pipelines. Clarification of phenomena in curved flows involving inherent unstable and stable mechanisms is therefore of great importance.

The mean velocity profile in wall turbulence subject to a streamline curvature has been experimentally studied by many researchers. Wattendorf [1] observes a region with a constant angular momentum, i.e., $rU_\theta = const.$ (where U_θ is the streamwise mean velocity and r denotes the radial position) in a turbulent curved channel flow with a strong curvature, i.e, $\delta/R_c = 0.1$ (where δ is the channel half width and R_c is the radius of curvature). On the other hand, Hunt and Joubert [2] do not observe such a region with constant angular momentum in the case of weak curvature ($\delta/R_c = 0.01$). The mean velocity profile in the vicinity of a curved wall is similar to that of a plane wall [3, 4].

*Author to whom correspondence should be addressed. Present address: Toyota Central Research Laboratories, 41-1 Yokomichi, Nagakute, Nagakute-cho, Aichi 480-1192, Japan. E-mail: e1263@mosk.tytlabs.co.jp (M. Nagata)

Table 1: Computational conditions. (The mesh size is in the local wall unit evaluated after the simulation.)

Case	δ/R_c	Re_τ	$(r\Delta\theta)^+$	Δr^+	Δz^+
			convex - concave	convex - center	convex - concave
Case 1	0.013	150	15.60 - 19.53	0.16 - 6.07	6.27 - 7.84
Case 2	0.05	150	14.57 - 20.62	0.15 - 6.41	5.85 - 8.28
Case 3	0.1	150	13.98 - 20.83	0.15 - 6.48	5.61 - 8.37
Case 4	0.2	150	13.37 - 19.77	0.14 - 6.15	5.37 - 7.94

Away from the wall, the mean velocity is higher on the convex side and lower on the concave side, respectively, as compared to that on a plane wall [1, 5–7].

Turbulent stresses are also modified by the streamwise curvature. So and Mellor [6] show that the turbulent motion substantially disappears in a half of boundary layer near the convex wall with strong curvature ($\delta/R_c = 0.05 \sim 0.1$). Gillis and Johnston [7] demonstrate that all the turbulent shear stress components collapse into a single curve when normalized by the friction velocity. So and Mellor [6] also observe an enhancement of the turbulent motion on a concave boundary layer with a strong curvature. The turbulence intensity near the concave wall is almost twice as large as that on a corresponding plane wall. The vanishing point of the turbulent shear stress is located at $y/\delta = 1.1$. In the region near the wall, the turbulent shear stress normalized by the turbulent energy is nearly the same as that of the plane channel flow. Similar enhancement and suppression of turbulence intensity are observed in fully-developed turbulent curved channel flows [2, 5]. In channel flows, the point where the turbulent shear stress becomes zero shifts toward the convex side.

Despite those interesting and practically important observations, the underlying mechanisms have not fully been understood. As is the case with the plane turbulent channel flow, deeper understanding on the physics can be obtained by direct numerical simulation (DNS). To the best of authors' knowledge, there is only one published work on DNS of turbulent flow in a channel with streamwise curvature, i.e., the paper by Moser and Moin [8]. Their conclusions on the turbulence statistics are that most of the quantities, except for the Reynolds shear stress, are similar to those in a plane channel flow when scaled with the proper local variables. Their DNS, however, is limited to a case of weak curvature ($\delta/R_c = 0.013$). Therefore, systematic knowledge with respect to the change of curvature is lacking. Dynamical production-dissipation mechanisms, which cause the modification of turbulence structure, are also still unclear.

In the present study, DNS of fully developed turbulent curved channel flow is performed for different radii of curvature in order to obtain the systematic knowledge on the effects of curvature to a turbulent channel flow. A special focus is laid upon the production and dissipation mechanisms near the convex and concave walls. For that purpose, we extract some fundamental dynamics of the turbulence-producing eddies between stable (i.e., convex) and unstable (i.e., concave) regions by using a spatio-temporal linear stochastic estimation.

2 DNS of turbulent curved channel flow

The governing equation for the fluid is the incompressible Navier-Stokes equation with the contravariant velocities on a generalized coordinate system. A second order central difference scheme is used for the spatial discretization on a staggered grid system. All the terms are advanced in time with the Crank-Nicolson method and the coupling between continuity and momentum equations is treated by using the fractional step method, similarly to Choi *et al.* [9]. No-slip boundary condition is imposed

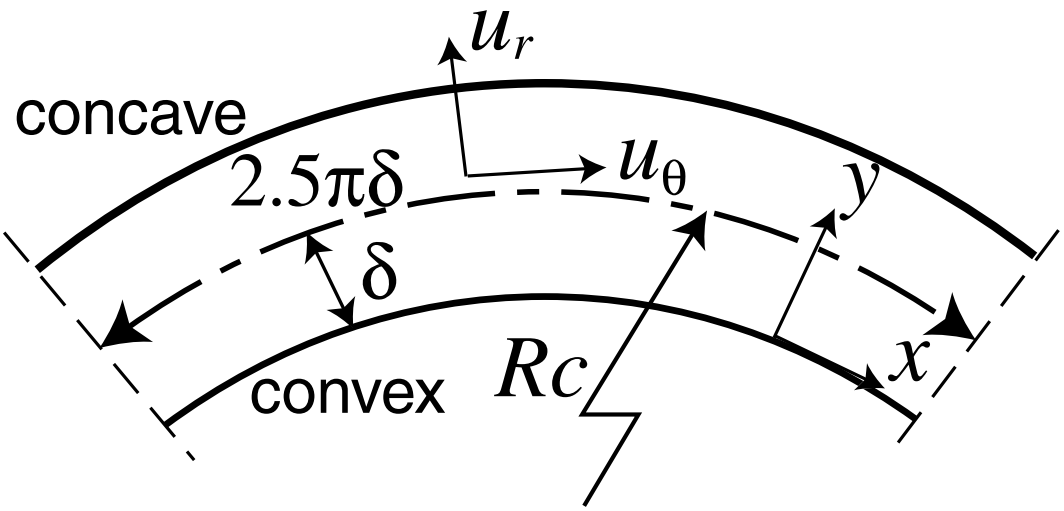

Figure 1: Computational domain.

on the walls. The flow is driven by a constant mean pressure gradient. Namely, the friction Reynolds number, $Re_\tau = u_\tau\delta/\nu$, is set constant. From the balance between the mean pressure gradient and wall shear stress, the global friction velocity u_τ, can be defined, using the friction velocity on the convex wall $u_{\tau i}$ and that on the concave wall $u_{\tau o}$, as

$$u_\tau = \sqrt{\frac{R_i^2 u_{\tau i}^2 + R_o^2 u_{\tau o}^2}{2R_c^2}}\,, \tag{1}$$

where R_i, R_o and R_c are the radii of curvature at the convex wall, the concave wall and the channel centerline, respectively.

The temperature is treated as a passive scalar and iso-heat flux condition is imposed at the walls, similarly to Kasagi *et al.* [10]. The mean heat flux, q_w, is defined as

$$q_w = \frac{q_{wi}R_i + q_{wo}R_o}{2R_c}\,, \tag{2}$$

where q_{wi} and q_{wo} are the heat fluxes on the convex and concave walls, respectively.

The computational domain is shown in figure 1, where δ is the channel half-width and R_c is the radius of curvature at the channel centerline. Four different radii of curvature are tested, as listed in table 1. The computational domain is $2.5\pi\delta \times 2\delta \times \pi\delta$ and is covered by $64 \times 128 \times 64$ grid points; in the streamwise, wall-normal and spanwise directions, respectively. The grid spacing in the streamwise and spanwise directions are $R_c\Delta\theta^+ = 18.3$ and $\Delta z^+ = 7.35$ in wall units. Non-uniform meshes are used in the radial direction. The first mesh point away from the wall is $\Delta r^+ (= \Delta y^+) = 0.19$, and the maximum spacing (at the centerline of the channel) is about 5 wall units. Although the local Reynolds number on the concave side increases as the curvature becomes larger, the grid spacing is kept nearly the same, as shown in table 1.

Figure 2 shows instantaneous isosurfaces of the streamwise vorticity in an $r-\theta$ cross-section computed for different radii of curvature. Even with the weakest curvature examined (figure 2(a)), vortices on the convex side are attenuated due to the centrifugal stabilizing effect. As the curvature increases, the attenuation becomes more pronounced. In the case of strong curvatures (figure 2(c)-(d)), the vortical structure, that has been developed and stretched in the streamwise direction on the concave side, extends over the center region of channel. In contrast, the vortices are scarcely detected on the convex side.

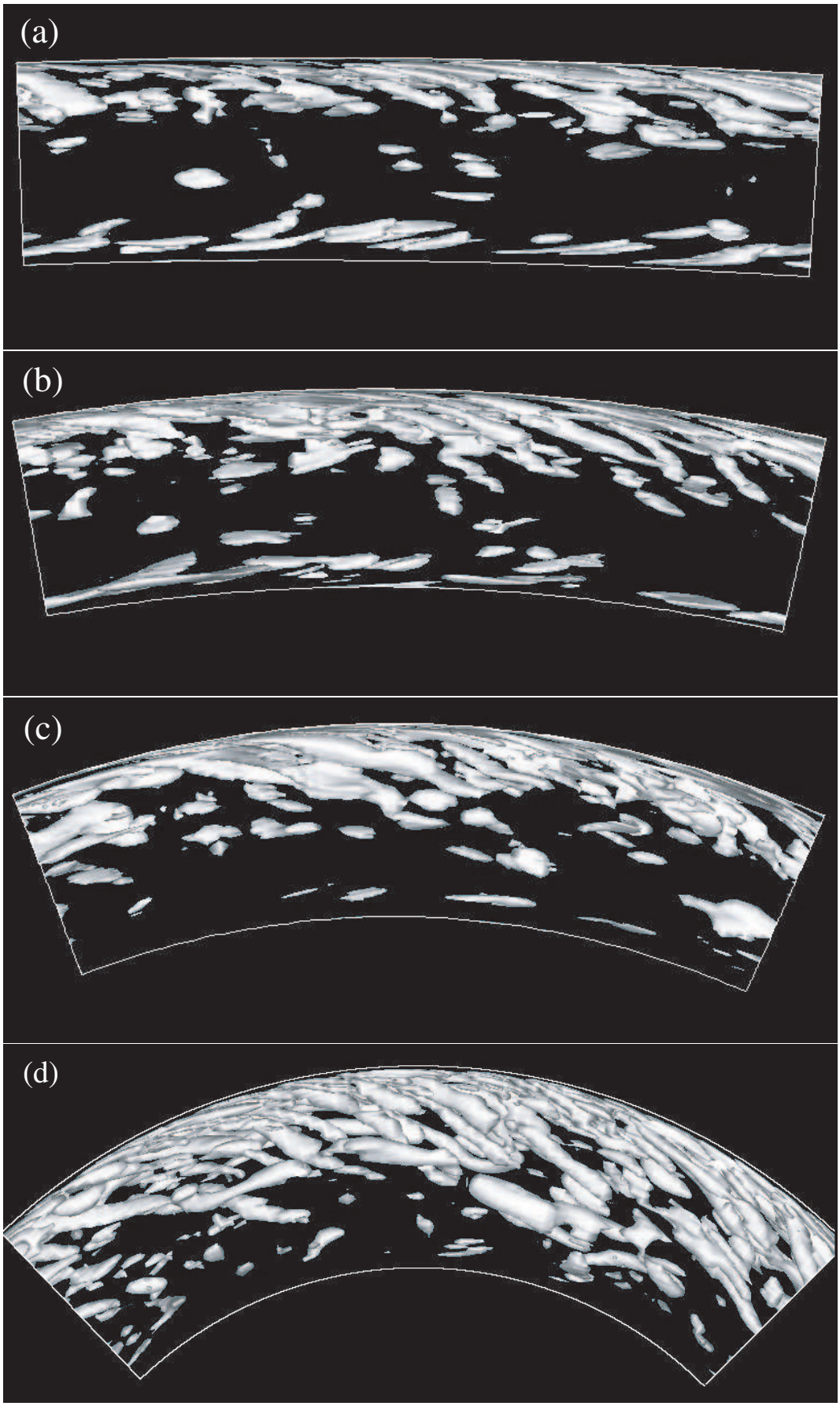

Figure 2: Isosurfaces of instantaneous streamwise vorticity ($\omega_x \delta / u_\tau = 30$). (a) $\delta / R_c = 0.013$; (b) $\delta / R_c = 0.05$; (c) $\delta / R_c = 0.1$; (d) $\delta / R_c = 0.2$. **[link to AVI file "fig2d.avi"]**

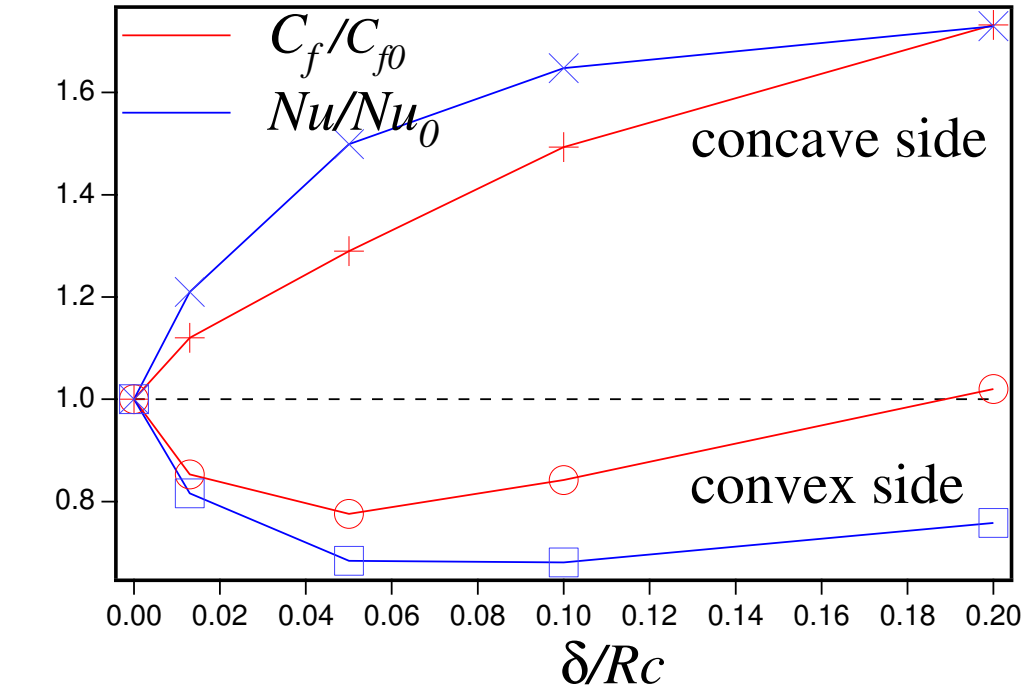

Figure 3: Skin friction coefficient (C_f) and Nusselt number (Nu)for different radii of curvature (δ/R_c).

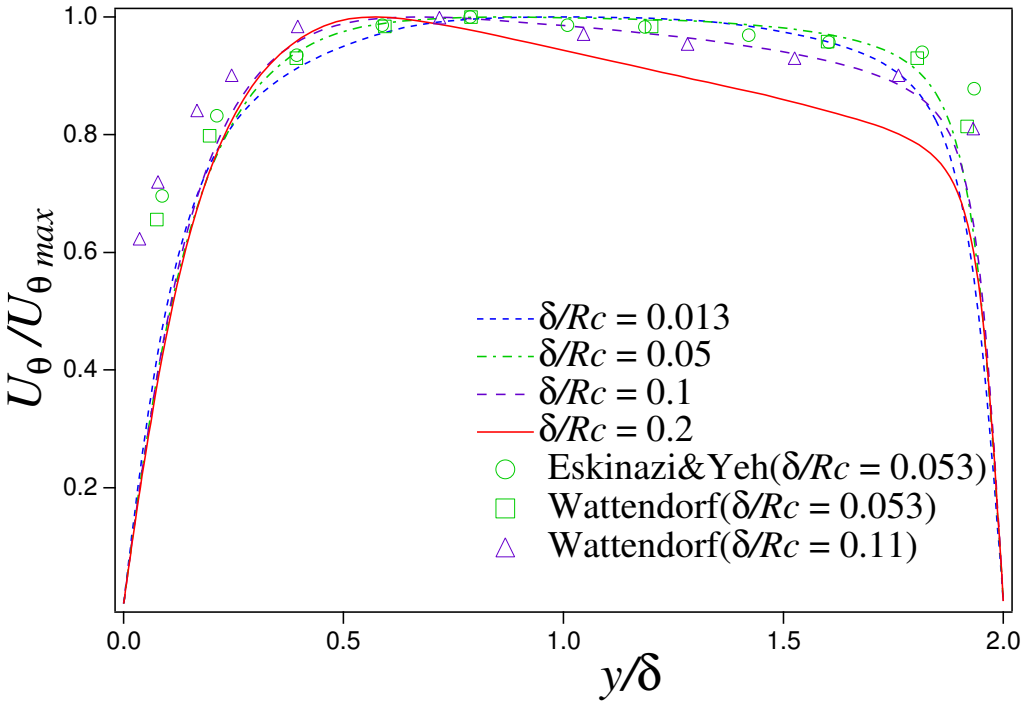

Figure 4: Mean velocity profile.

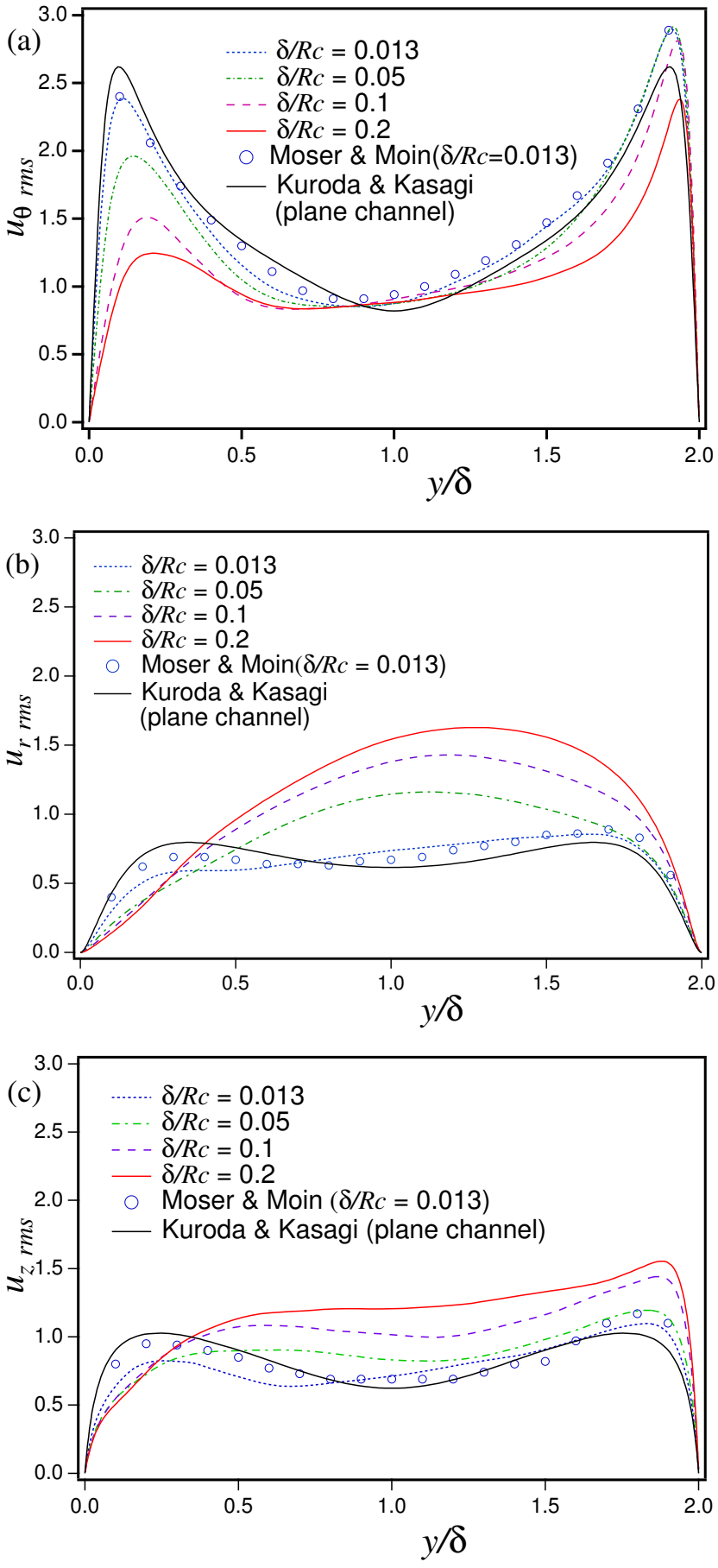

Figure 5: Turbulence intensity distributions. (a) streamwise component; (b) radial component; (c) spanwise component.

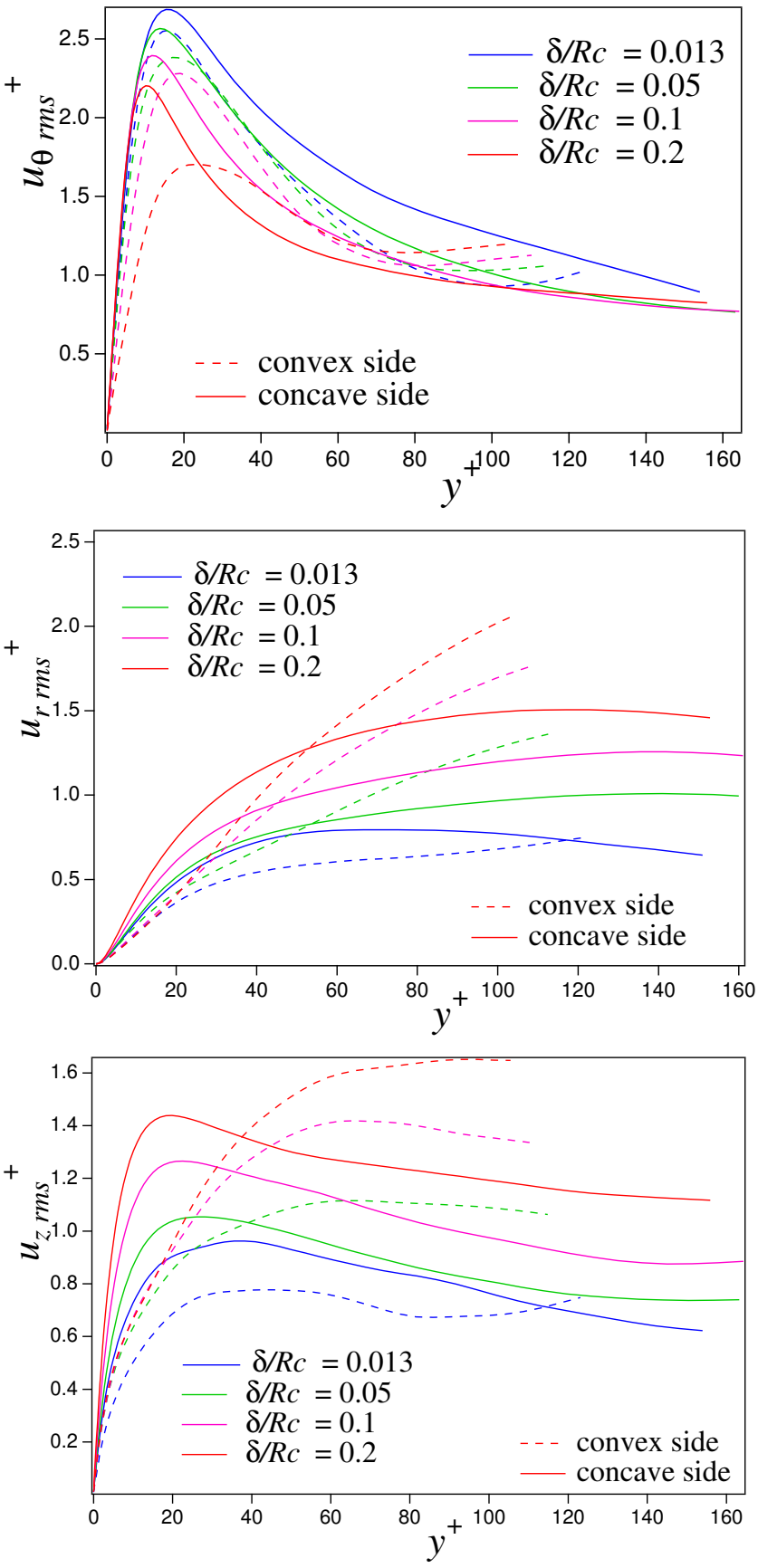

Figure 6: Rms velocity in local wall coordinates. (a) streamwise component; (b) radial component; (c) spanwise component.

3 Turbulence statistics

3.1 Mean statistics

First of all, the skin friction coefficient, i.e., $C_f = 2\tau_w/(\rho < u_\theta >^2)$, and the Nusselt number, i.e., $Nu = 2hd/\lambda$ (where $h = q_w/(T_w - [T])$), are presented in figure 3 as a function of the curvature. Here, $< \cdot >$ denotes the integral mean value in the channel and $[\cdot]$ denotes the mean value in a region from each wall to a point where the maximum value is located. The quantities used for normalization, i.e., C_{f0} and Nu_0, are those of a channel flow at the same friction Reynolds number. As the curvature increases, the friction coefficient increases on the concave side due to the centrifugal instability effect, whereas it decreases on the convex side. The Nusselt number shows a similar trend, but the rate of change is generally larger than that of the friction coefficient.

The mean velocity profile is shown in figure 4. It is non-dimensionalized with the maximum mean velocity in order to compare with the available experimental data. In accordance with the experimental observations [1,5], there is a region in the center of the channel where the angular momentum becomes constant when the curvature is strong, and such region is unclear when the curvature is weak. The experimental data corresponds well to the present DNS calculations in the channel center region, however, the discrepancy is seen in the convex side. This appearance is originated from the difference of Reynolds number. The experiments are conducted in at least ten times lager Reynolds number (Re_b is the order of 10^4) than the present DNS (Re_b is the order of 10^3). The low Reynolds number flow subjected to stronger curvature effect results in lower velocity and wall shear stress on the convex side. In other words, the flow at low Reynolds number feels the curvature effect more strongly.

3.2 Reynolds normal stresses and budgets

Figure 5 shows the root-mean-square (rms) velocity fluctuations. In the case of $\delta/R_c = 0.013$, the profiles are in fair agreement with those presented by Moser and Moin [8]. Small quantitative differences is likely due to the difference in the Reynolds numbers, i.e., $Re_\tau = 168$ in [8] and $Re_\tau = 150$ in the present study. The relative magnitude of curvature that the flow *feels* may be larger with a lower Reynolds number, as mentioned above. As the curvature increases, the streamwise rms velocity is reduced on the convex side due to the centrifugal stabilizing effect. At the same time, the radial and spanwise rms velocities increase in the center region. The radial rms velocity eventually exceeds the streamwise component when the curvature is larger than 0.05. The rms velocities are also presented as functions of distance in wall units (figure 6). The peak location of the streamwise and spanwise rms velocities on the concave side shift towards the wall as the increase of the curvature, whereas those on the convex side a shift towards the center. The magnitude of all the components are significantly modified as the curvature becomes strong. This observation suggests a strong dependency of the turbulence intensity near the wall on the curvature, in contrast to the conclusions drawn by Moser and Moin [8].

In order to explain the increase of the radial and spanwise rms velocities in the center region, the effect of curvature on the production of Reynolds normal stresses is investigated. Here, we calculate the flux Richardson number, R_f, which was originally proposed by Bradshaw [11] to represent the buoyancy effect in the stratified flow . In the present study, R_f is defined by the ratio of the production by the centrifugal force to the shear production. The streamwise and radial production terms can be written as

$$P_{\theta\theta} = -2\left[\overline{u_\theta u_r} r \frac{\partial(U_\theta/r)}{\partial r} + 2\overline{u_\theta u_r}\frac{U_\theta}{r}\right] \tag{3}$$

and

$$P_{rr} = 4\overline{u_\theta u_r}\frac{U_\theta}{r}\,, \tag{4}$$

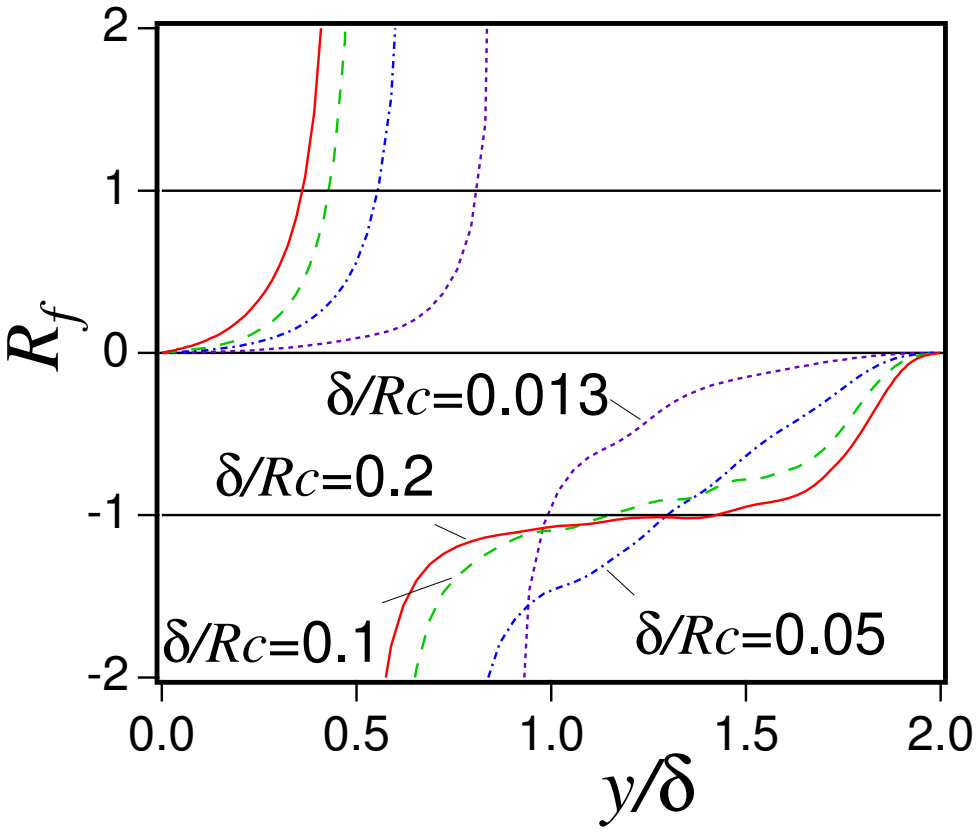

Figure 7: Flux Richardson number distributions.

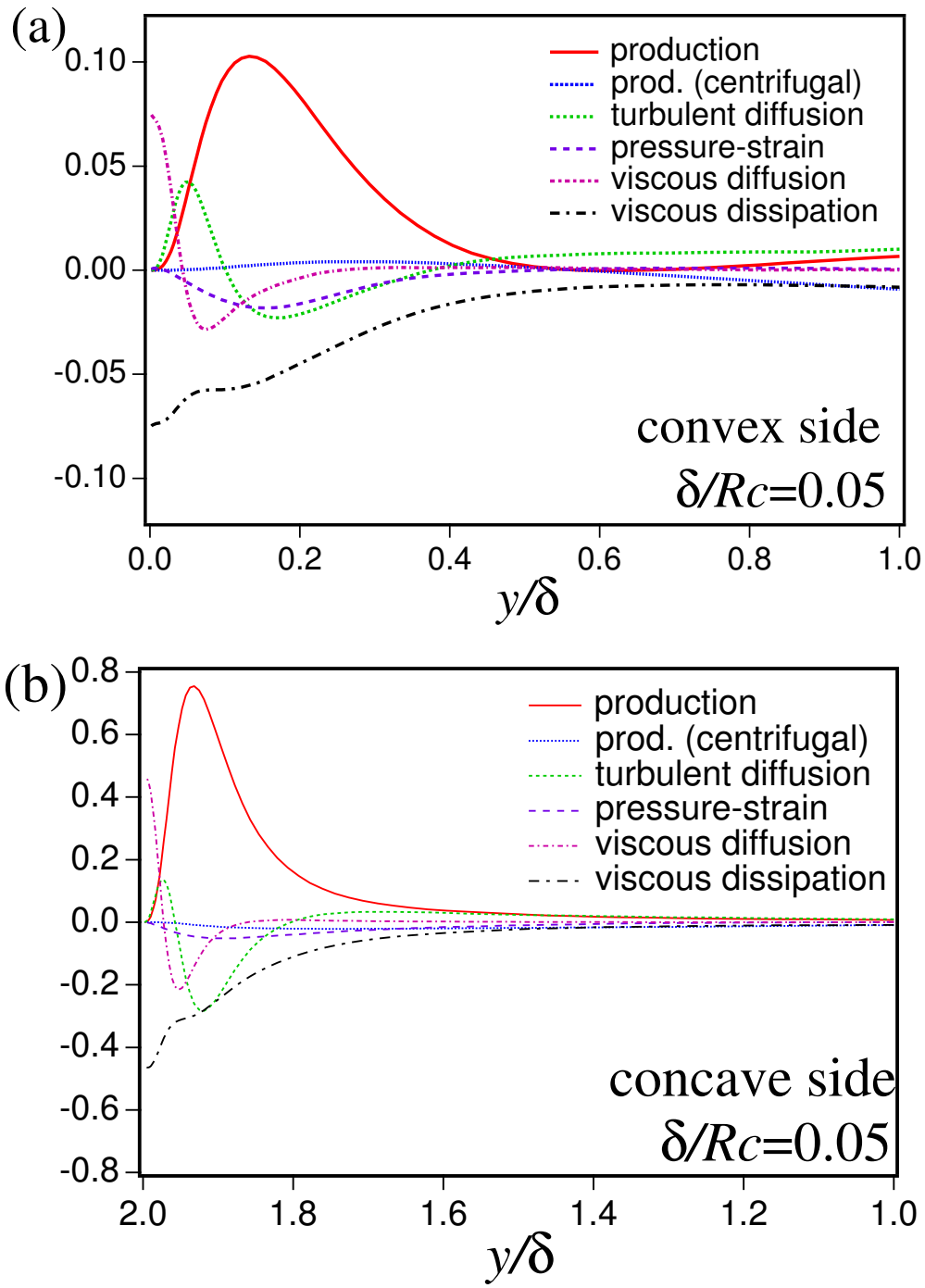

Figure 8: Budget of streamwise Reynolds normal stress, $\overline{u_\theta u_\theta}$. (a) convex side; (b) concave side.

respectively. Here, the first term in the right-hand-side of (3) represents the shear production (hereafter referred to as SP). The second term of (3) and the right-hand-side of (4) are the centrifugal production (CP). Therefore, the flux Richardson number can be defined as

$$R_f = \frac{2U_\theta/r}{r[\partial(U_\theta/r)/\partial r]} \ . \tag{5}$$

Note that the second term of (3) has the same absolute value as (4) with an opposite sign. These terms represent the redistribution between the streamwise and radial Reynolds stress components due to the centrifugal effect. The flux Richardson number can therefore be interpreted also as the ratio of redistribution to shear production. Note also that CP is identical to the summation of *streamwise production* and *convection* referred to as in [8]. As shown in figure 7, R_f is positive on the convex side and negative on the concave side. Namely, the redistribution occurs from the radial to streamwise components on the convex side and from the streamwise to radial components on the concave side. In the center region, R_f is less than -1 when the curvature is larger than 0.05. In those cases with strong curvature, the energy transfer from the streamwise to radial components (i.e., CP) exceeds SP, so that the radial rms velocity becomes larger than the streamwise rms velocity in the center region, as observed in figure 5(b).

The budget of streamwise Reynolds stress $\overline{u_\theta u_\theta}$ in the case of $\delta/R_c = 0.05$ is shown in figure 8. The changes from a plane channel are qualitatively similar to those in the case of weak curvature [8]. The amount of changes, however, is one order larger. SP and turbulent diffusion (TD) are enhanced on the concave side due to the centrifugal instabilizing effect, whereas those on the convex side are suppressed. Although CP is small near the wall, it has a comparable magnitude as SP in the center of channel. Figure 9 presents the budget of radial (i.e., wall-normal) Reynolds stress $\overline{u_r u_r}$. In a plane channel flow, the main source for the gain is the velocity-pressure gradient (i.e., the pressure strain (PS) plus the pressure diffusion (PD)) and that for the loss is the dissipation (D) (Mansour *et al.* [12]). In the present case, CP has a comparable magnitude as PS, PD and D in the entire region and is negative near the convex wall and positive near the concave wall. Especially, CP is a main contributor to the radial Reynolds stress budget on the concave side and the value of CP exceeds that of PS. This also explains the prominence of radial rms velocity in the center region. Accompanied with the additional mechanism of production (i.e., CP), TD is also enhanced in the entire region. The budget of spanwise Reynolds stress is depicted in figure 10. Similarly to the plane and weakly curved channels, PS acts as the main contributor to the gain, although it is weakened on the convex side and enhanced on the concave side. In the region away from the convex wall ($y/\delta \sim 0.8$), the main contributor is replaced to TD. The increase of redistribution from the radial component on the concave side and the enhanced TD raise the spanwise turbulence intensity in the center region. Furthermore, the increase of PS and TD with increasing the curvature results in the enhancement of the spanwise turbulence intensity(not shown here). This tendency originates in the increased redistribution from the radial component.

3.3 Contribution to Reynolds shear stress

Detailed information on the contribution of various combinations of positive and negative u_θ and u_r to the turbulent stress production can be obtained by the quadrant analysis of the Reynolds shear stress (Wallace *et al.* [13]). Figure 11 shows the contribution of each quadrant on the convex side in the case of $\delta/R_c = 0.05$. Here, y^+ denotes the local wall coordinate on the convex side. The fourth quadrant (Q4) is the main contributor to the Reynolds shear stress in the entire region of the convex side. This implies that the turbulent motion on the stable side is maintained by the inflow of high-speed fluids. Figure 12 presents the quadrant analysis on the concave side. Similarly to the case of plane channel [14], Q4 give the largest contribution to the Reynolds shear stress only in the region

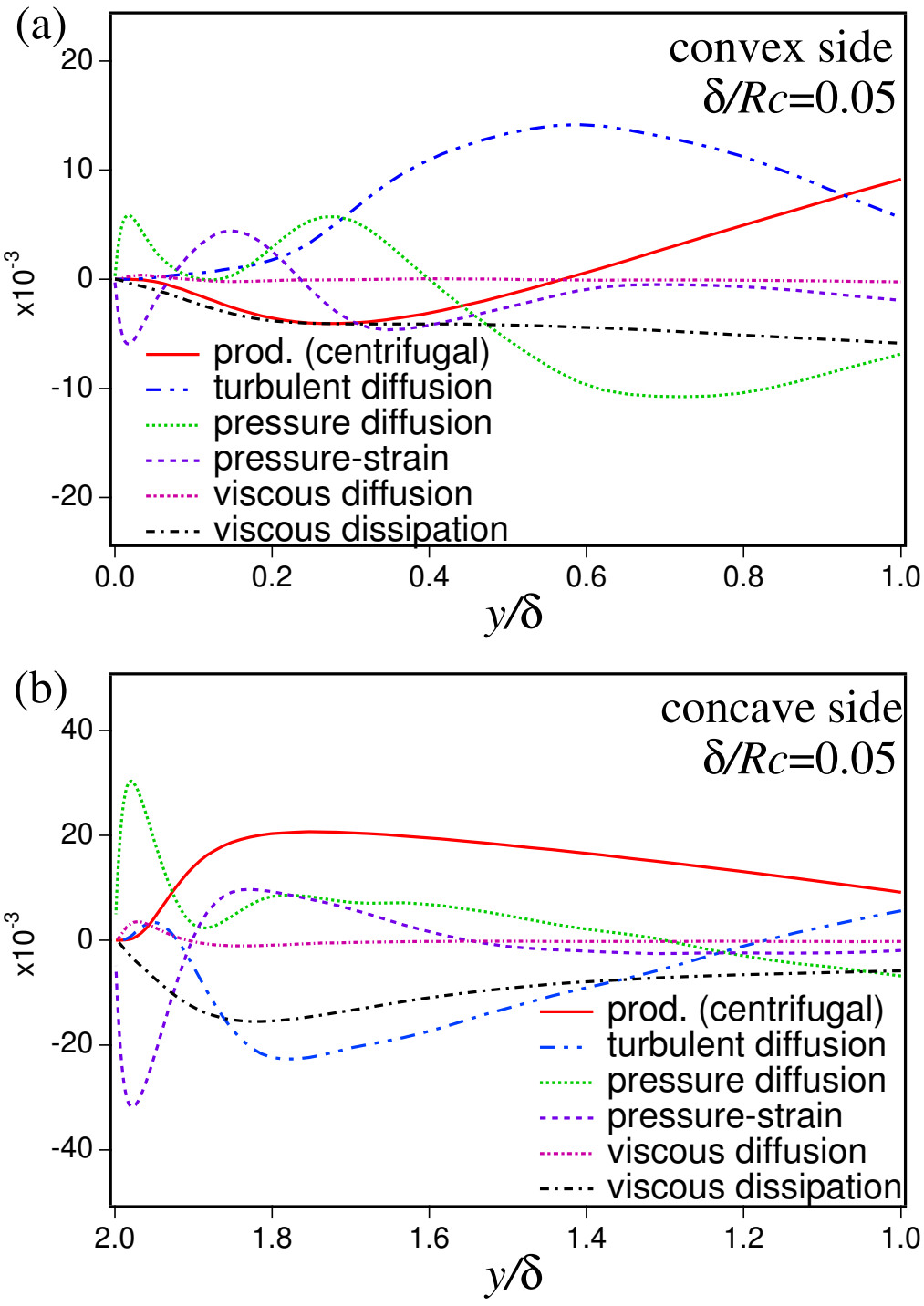

Figure 9: Budget of wall-normal Reynolds normal stress, $\overline{u_r u_r}$. (a) convex side; (b) concave side.

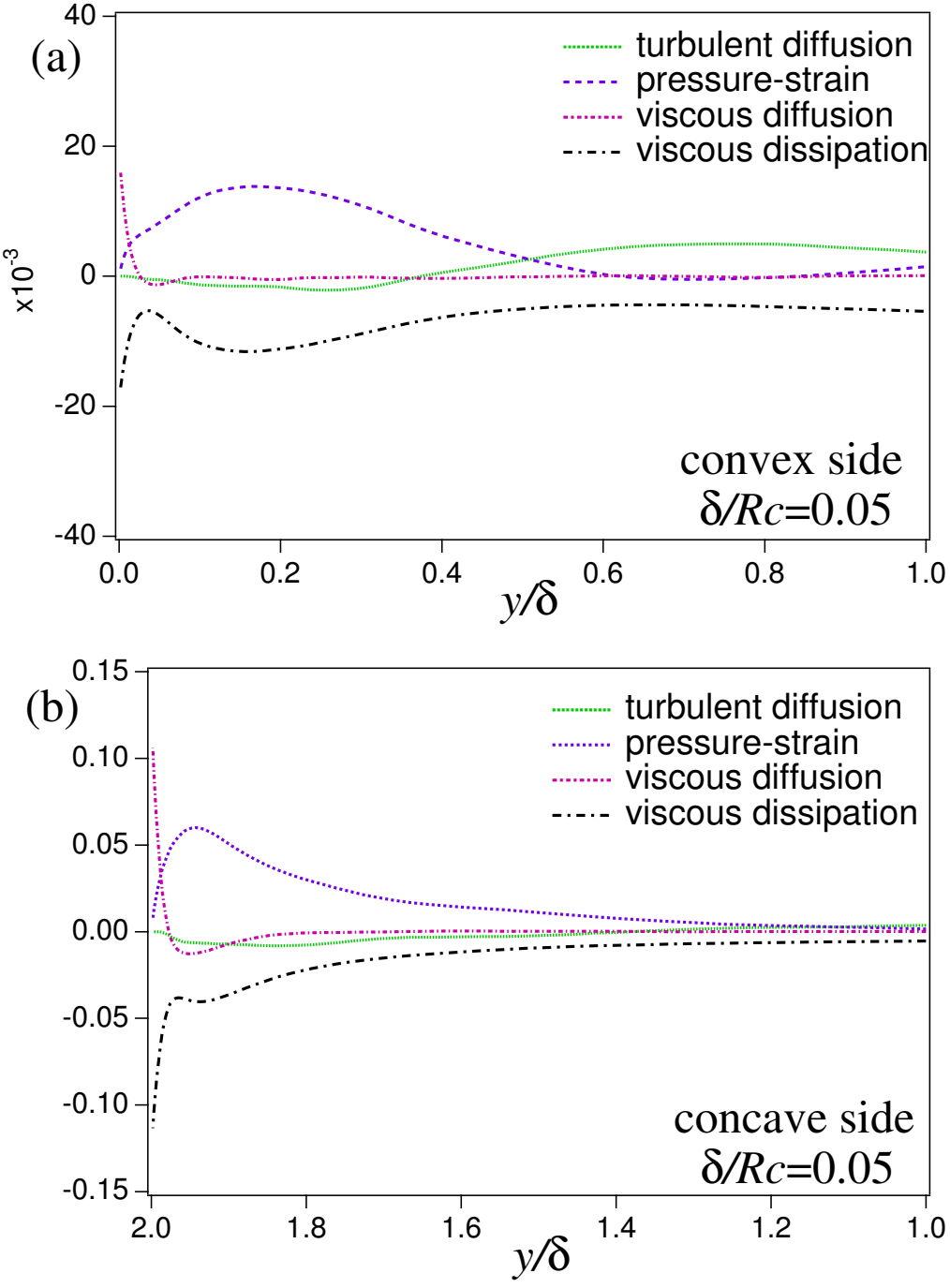

Figure 10: Budget of spanwise Reynolds normal stress, $\overline{u_z u_z}$. (a) convex side; (b) concave side.

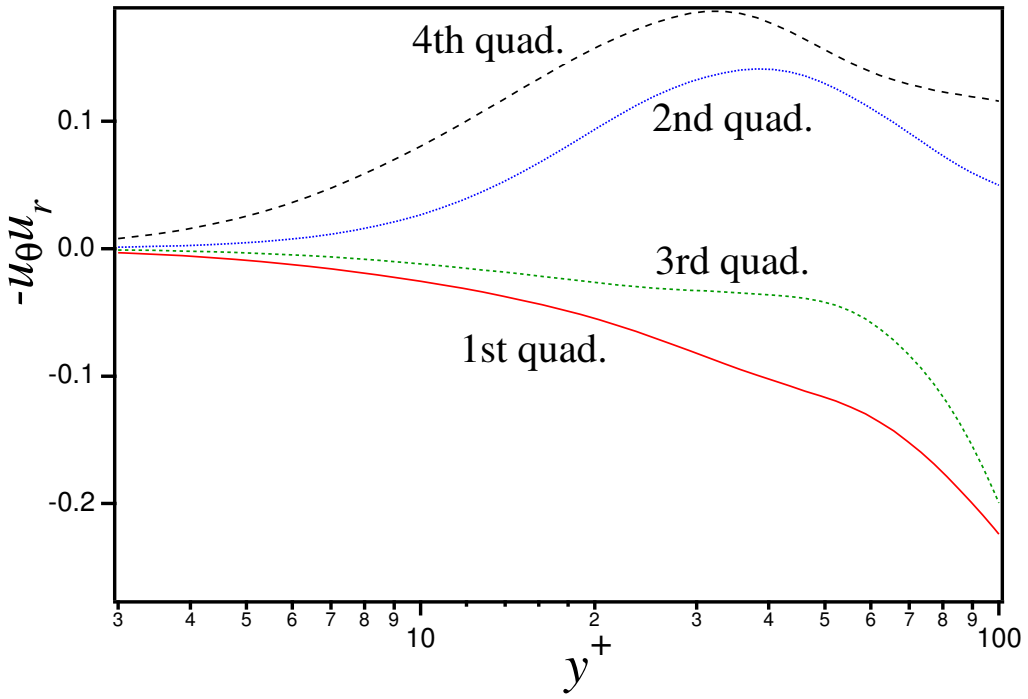

Figure 11: Quadrant analysis on convex side ($\delta/R_c = 0.05$).

near the wall, whereas the second quadrant (Q2) acts as the main contributor in the other region, i.e., $y^+ > 12$. On the convex side, the contribution of Q2 and Q4 is comparable to that of the first (Q1) and third (Q3) quadrants. On the concave side, Q2 and Q4 give much larger contribution than Q1 and Q3.

Figure 13 shows the joint probability density function (JPDF), $f(u_\theta, u_r)$, on the convex and concave walls. Here, the velocity fluctuations are normalized by their standard deviations. The correlation is weak on the convex side, whereas a strong negative correlation appears on the concave side due to the high possibility of occurrence of Q2 and Q4 motions. The contribution to the Reynolds shear stress (figure 14) explains the situation more clearly. The contribution, $u_\theta u_r f(u_\theta, u_r)$, is related with JPDF by

$$\overline{u_\theta u_r} = \int\int u_\theta u_r f(u_\theta, u_r) du_\theta du_r \,. \tag{6}$$

On the convex side, there is nearly equally large contribution from the Q2 and Q3. On the concave side, the contribution from Q2 and Q4 is dominant. This analysis confirms that there is an inherent mechanism which enhances the turbulence production on the concave wall.

4 Spatio-temporal linear stochastic estimation

4.1 Estimation procedure

The Linear Stochastic Estimation (LSE) (Adrian [15]) is a statistical estimation procedure to extract the representative flow structure for a given velocity condition around a sample point. The features of this method are: a) high convergency of the estimated field; b) statistical definiteness; c) flexibility to assign various conditional velocities. LSE has been applied to the plane boundary layer, turbulent pipe flow, round jet, isotropic turbulence and turbulent channel flow [15–17] and similar structures have been obtained to those by the other conventional conditional averaging methodology. Moreover,

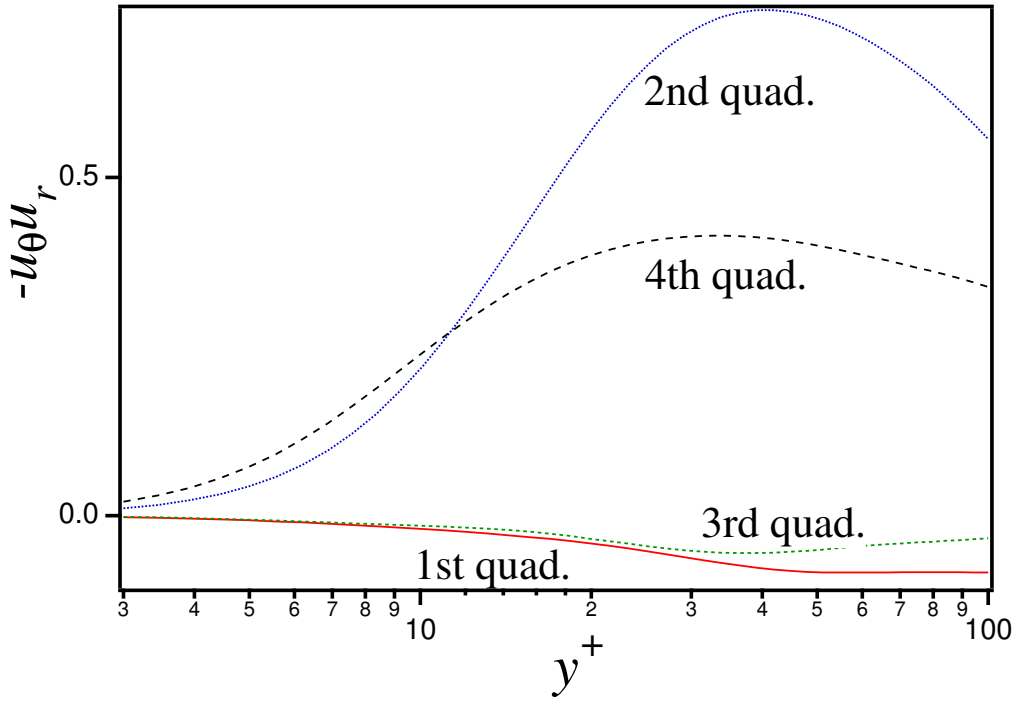

Figure 12: Quadrant analysis on concave side ($\delta/R_c = 0.05$).

LSE has been used to generate a *seed* for an investigation on the development process of fundamental vortical structure in a shear flow [18], or to reconstruct the velocity field from the pressure information [19] in combination with the proper orthogonal decomposition [20]. These studies demonstrate that the structure extracted by LSE well represents the essential feature of the vortical structure in turbulence, although it may also be viewed as a statistical artifact.

In this study, LSE is extended to a spatio-temporal version in order to extract the temporal developing/decaying process of the turbulence producing eddies formed between the stable (convex) and unstable (concave) sides. With this spatio-temporal LSE, the estimated velocity field, $\hat{u}_i$, is represented by the velocity condition, u_{cj}, through the linear combination, which reads

$$\hat{u}_i(\mathbf{x}', \tau; \mathbf{x}, t) = A_{ij} u_{cj}(\mathbf{x}, t) \ . \tag{7}$$

The vector $\mathbf{x}$ denotes the point where the velocity condition is imposed, $\mathbf{x}'$ is the location relative to $\mathbf{x}$, the scalar t is the time when the velocity condition is given and τ is the elapsed time from t. A location of $y^+ = 15$ is adopted as the velocity condition point $\mathbf{x}$ and the velocities which give the maximum contribution to Q2 and Q4 events are used as the velocity conditions, similarly to the spatial LSE of a plane channel flow by Moin *et al.* [17]. The curvature, δ/R_c, is set to 0.05 in which the radial turbulent intensity becomes larger than the streamwise component (figure 5). On the convex side, the velocities that give the maximum contribution to the Reynolds shear stress are $(u_\theta, u_r) = (-1.89, 7.99 \times 10^{-2})$ for Q2 and $(u_\theta, u_r) = (2.45, -0.176)$ for Q4. On the concave side, those are $(u_\theta, u_r) = (-5.64, 0.6)$ for Q2 and $(u_\theta, u_r) = (3.24, -0.2)$ for Q4. The estimation coefficient, A_{ij} in (7), is determined to minimize the least square difference between the velocity obtained by the conditional averaging and that estimated by (7). According to this procedure, the coefficient A_{ij} is obtained from the spatio-temporal two-point correlation of the velocity components. Hereafter, we refer to the velocity condition mentioned above as Q2 (or Q4) condition and the motion induced by that velocity condition as Q2 (or Q4) motion, and so on.

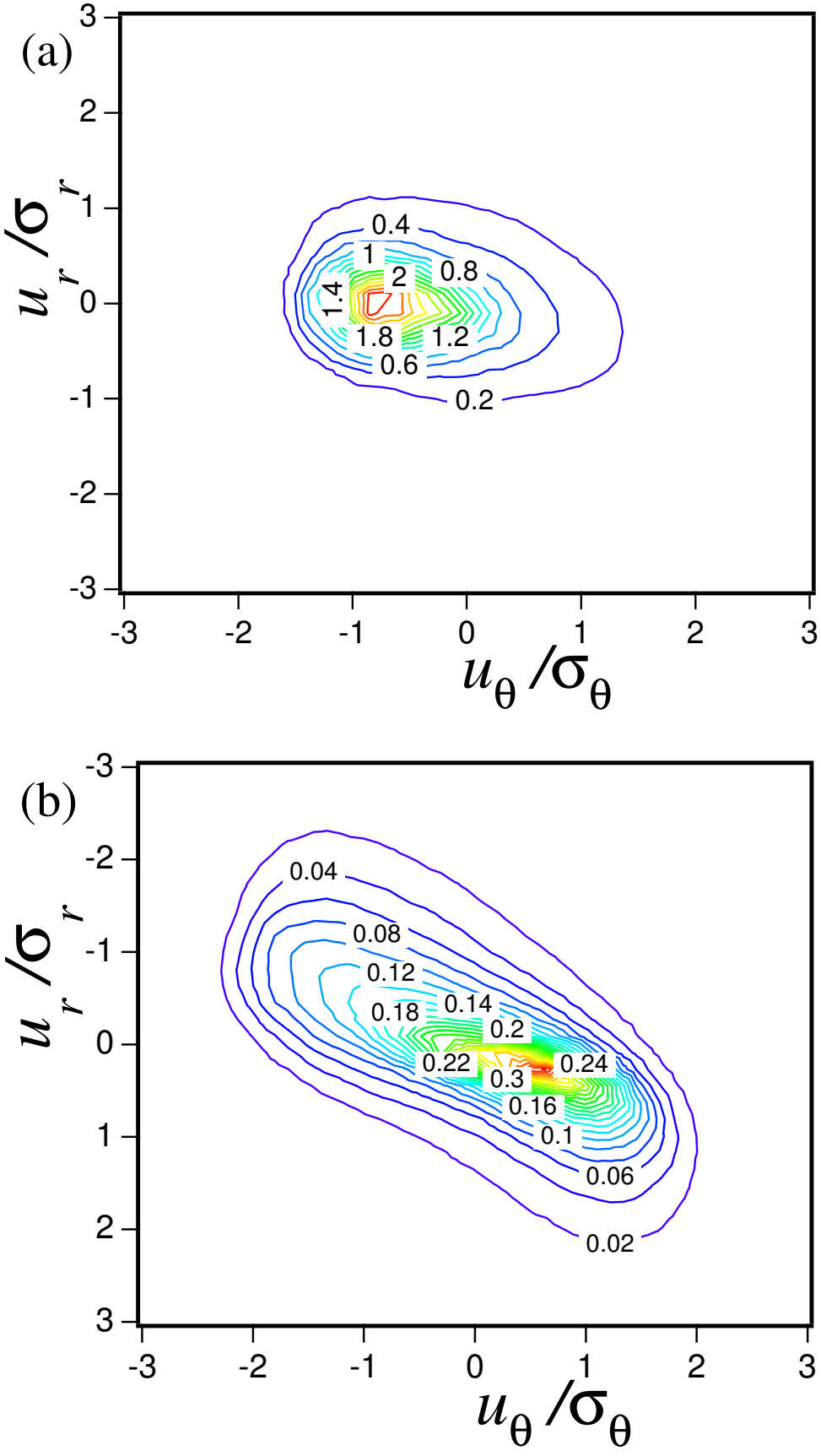

Figure 13: Joint probability density function at $y^+ = 13$ ($\delta/R_c = 0.05$). (a) convex side; (b) concave side.

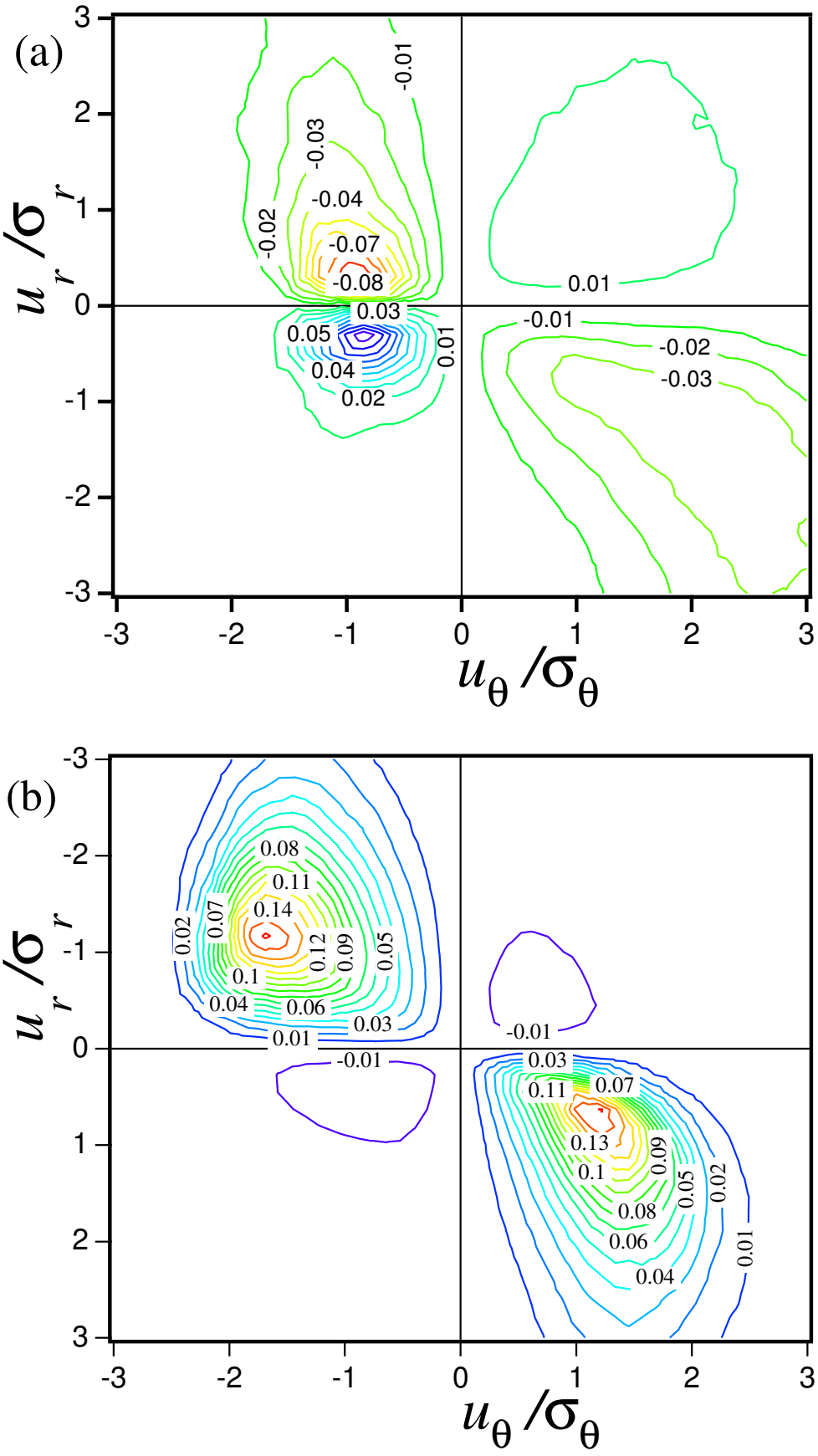

Figure 14: Contribution to the Reynolds shear stress at $y^+ = 13$ ($\delta/R_c = 0.05$). (a) convex side; (b) concave side.

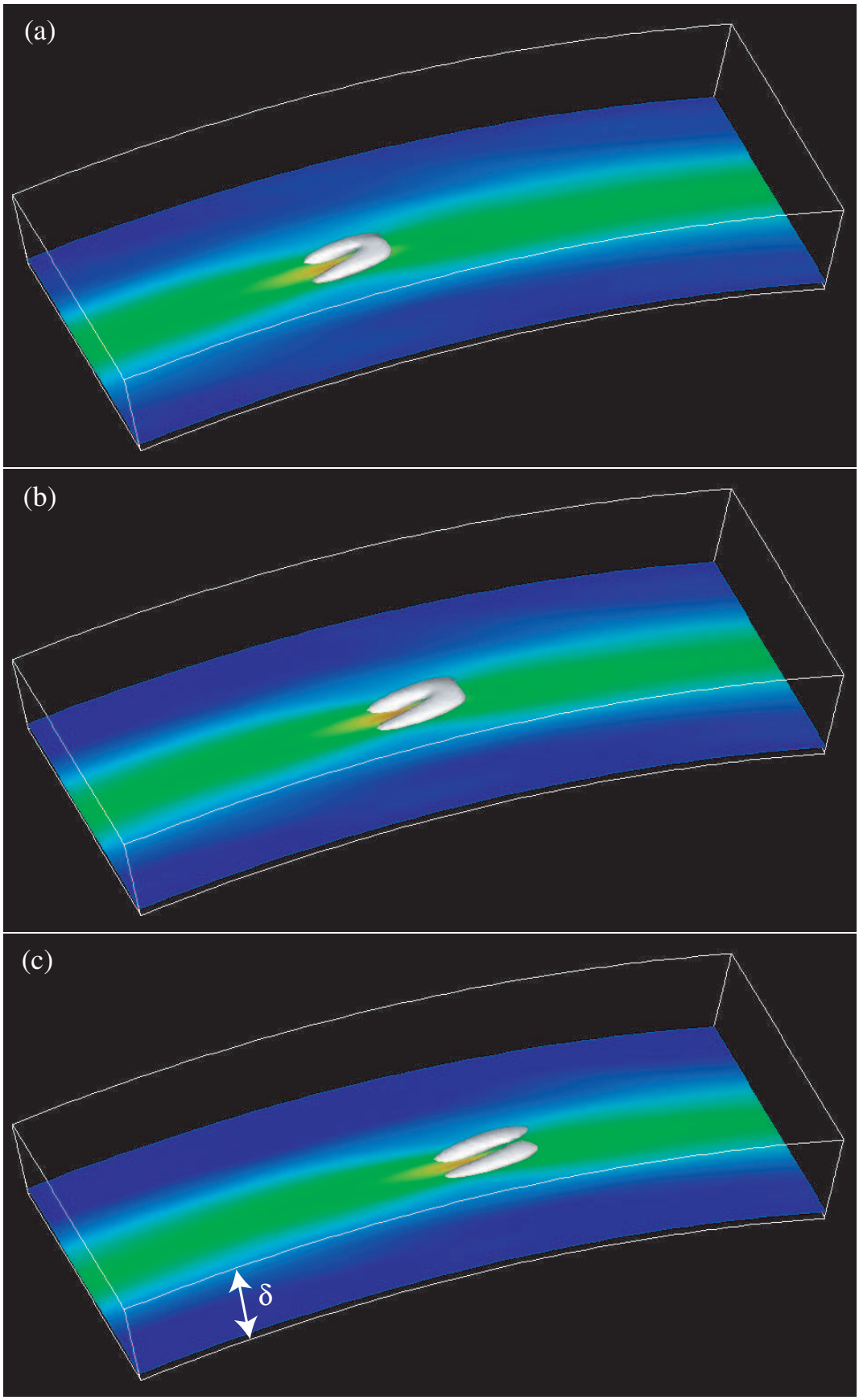

Figure 15: Time development of the fourth quadrant vortices and high speed region on the convex side ($\delta/R_c = 0.05$). (a) $\tau^+ = -10.5$; (b) $\tau^+ = 0$; (c) $\tau^+ = 10.5$. White, $II^+ = 0.22 \times 10^{-3}$; color, $\hat{u}_\theta$ from -2.4 to 2.4 ($y^+ = 10$). **[link to AVI file "fig15.avi"]**

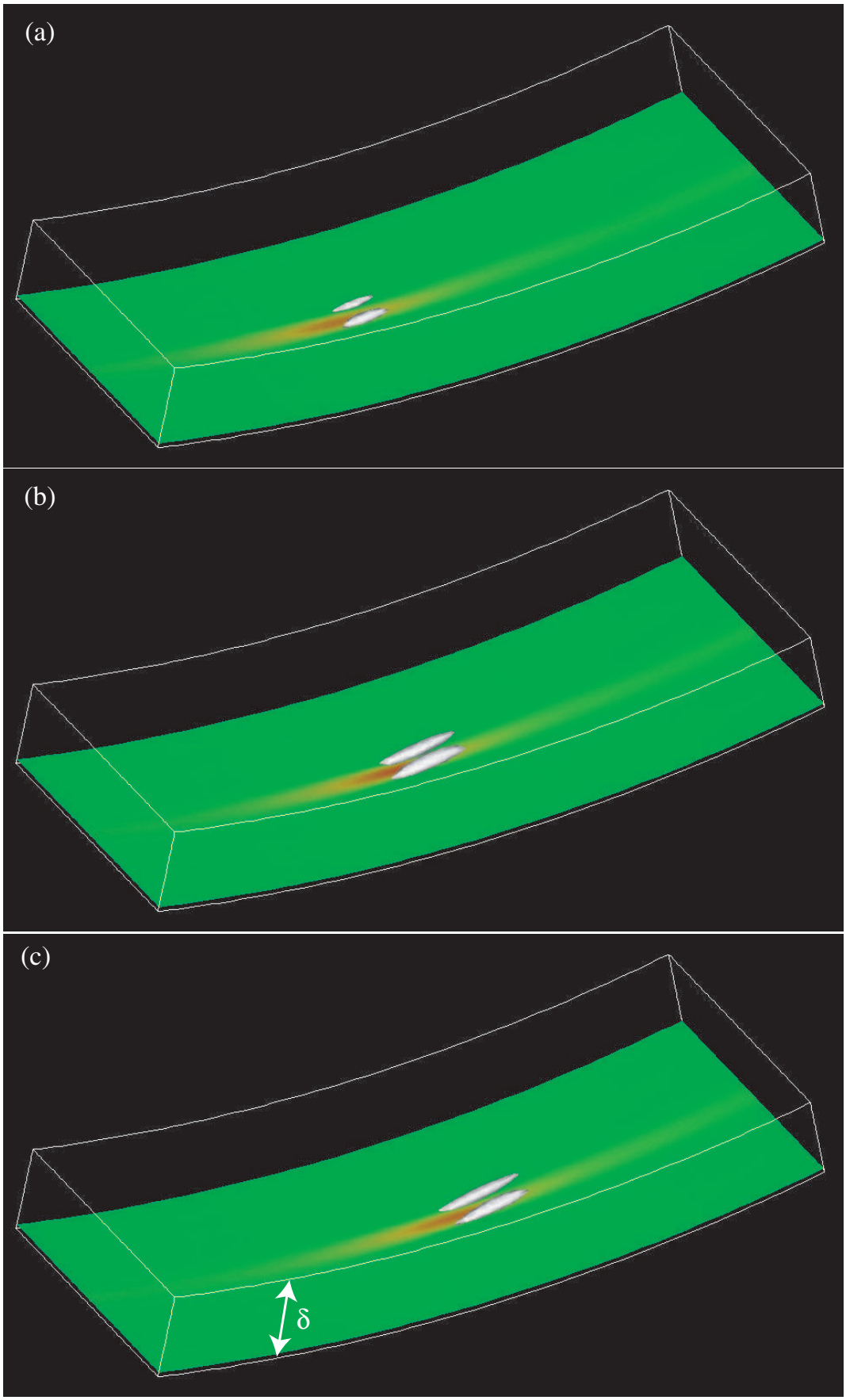

Figure 16: Time development of the fourth quadrant vortices and high speed region on the concave side ($\delta/Rc = 0.05$). (a) $\tau^+ = -10.5$; (b) $\tau^+ = 0$; (c) $\tau^+ = 10.5$. White, $II^+ = 0.44 \times 10^{-3}$; color, $\hat{u}_\theta$ from -3.22 to 3.22 ($y^+ = 10$). **[link to AVI file "fig16.avi"]**

4.2 Estimated spatio-temporal structure

The extracted temporal evolution of the Q4 vortices and high speed region on the convex side is illustrated in figure 15. Here, the vortices are identified by the second invariant of velocity deformation tensor, $II = u_{i,j}u_{j,i}$. A hairpin-like vortex is formed at $\tau^+ = -10.5$ (figure 15(a)) and maintained until $\tau^+ = 0$ (figure 15(b)). This vortical structure is similar to that observed in a plane channel [17]. Afterwards, the structure becomes a pair of streamwise vortices as a consequence of the attenuation of the hairpin-head. Then it is convected further downstream with decay. On the concave side (figure 16), a pair of streamwise vortices is formed from the beginning and developed until $\tau^+ = 0$ (figure 16(a)-(b)). The vortices become thinner as they are convected downstream (figure 16(c)). A high speed streak appears under the region between the streamwise vortices.

Figure 17 shows the estimated velocity vectors and the Reynolds shear stress in the $y' - z'$ cross-section (y', wall-normal direction; z', spanwise coordinate relative to the velocity condition point) on the convex side at $x' = 0$ and $\tau = 0$. The upper edge of figure 17 corresponds to the channel center plane and the bottom edge to the convex wall. With Q2 condition (figure 17(a)), a strong Reynolds stress is observed around the point where the velocity condition is given. Q2 motion, i.e., the motion directed away from the wall, can be seen at the same point. In the channel center region, a pair of large roll-cells is additionally observed. It appears that the strong upward motion is induced by the large organized vortices and this large-scale motion is essential for the turbulence on the convex side to be maintained against the centrifugal stabilizing effect. A similar feature is found with the Q4 condition, as shown in figure 17(b). Namely, a large-scale roll-cell in the channel center region is observed to make a strong downwash near the wall. In contrast to the convex side, large roll-cells are not observed on the concave side (either Q2 or Q4 condition), as shown in figure 18. Strong vortex motion such as roll-cell is not essential for the development of the Q2 and Q4 motions on the concave side. There is an inherent self-sustaining mechanism which enhances the turbulent motion.

In what follows, we investigate on the time variation of the estimated velocity along $z' = 0$ axis on the convex and concave walls. The estimated velocity is observed on a reference frame moving with the convective velocity that is determined through the spatio-temporal two-point correlation. Figure 19 shows the profiles of estimated streamwise velocity, $\hat{u}_\theta$, on the convex side at different times. Both with Q2 and Q4 conditions, the estimated streamwise velocity attains its maximum value at the time when the velocity condition is given ($\tau^+ = 0$) . Similar results are obtained on the concave side (figure 20). The profiles of estimated streamwise velocity at $\tau^+ = -10.5$ and $\tau^+ = -21$ are similar to those at $\tau^+ = +10.5$ and $\tau^+ = +21$, respectively. Namely, the estimated streamwise velocity evolution is nearly symmetric around $\tau^+ = 0$.

Figure 21(a) shows the time dependency of the radial velocity distributions on the convex side estimated with Q2 condition. The radial velocity at the earliest time ($\tau^+ = -21$) attains its maximum value in the center region ($y/\delta \sim 1.0$) and monotonically decreases as the time elapses. It implies that Q2 motion at $\tau^+ = 0$ is induced due to the strong outflow in the center region driven by the roll-cell at a prior time (i.e., $\tau^+ < 0$). Accordingly, the radial velocity in the near-wall region ($y/\delta \sim 0.2$) has a high value at the prior time ($\tau^+ < 0$), followed by the decay at $\tau^+ > 0$ owing to the centrifugal stabilizing effect. A similar tendency is observed for Q4 motion (figure 21(b)).

The time dependency of the estimated radial velocity on the concave side is shown in figure 22. In Q2 motion (figure 22(a)), the peak value of the radial velocity is not observed in the center region in contrast to that on the convex side. It is conjectured that the development of Q2 motion is more autonomic than that on the convex side. The radial velocity attains its peak value at $\tau^+ = 0$. By comparison between the curves at $\tau^+ = -21$ and $\tau^+ = 21$, we notice that the decaying process is milder than the development process. This is attributed to the constraint of the Q2 decaying motion affected by the centrifugal force, which should enhance the Q2 motion. Again, the trend is similar with the Q4 condition (figure 22(b)).

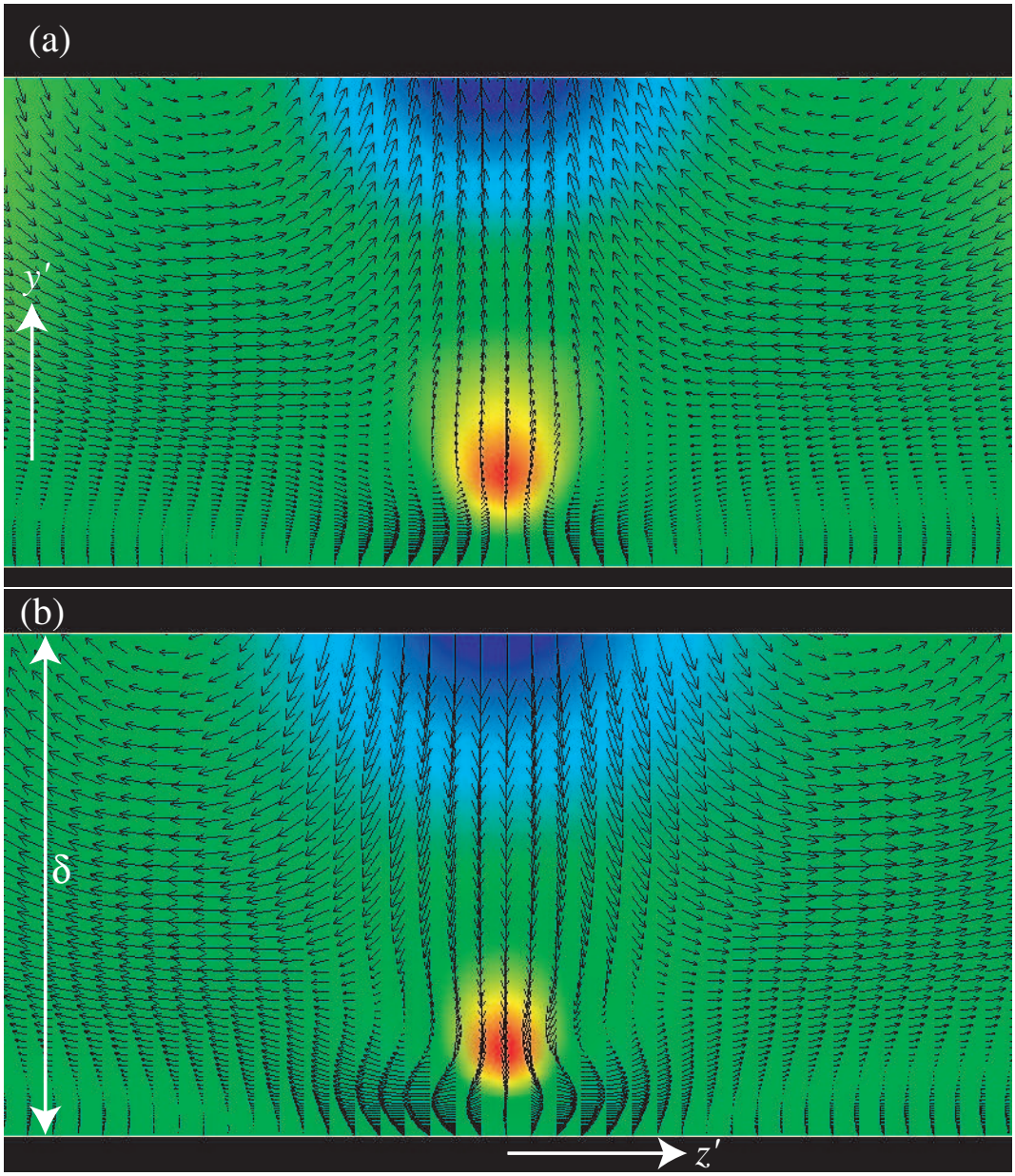

Figure 17: Estimated velocity vector $\hat{u}_r$, $\hat{u}_z$ and Reynolds stress $\hat{u}_\theta \hat{u}_r$ (color) on the convex side. (a) 2nd quadrant; (b) 4th quadrant; $\tau^+ = 0$, $x^+ = 0$.

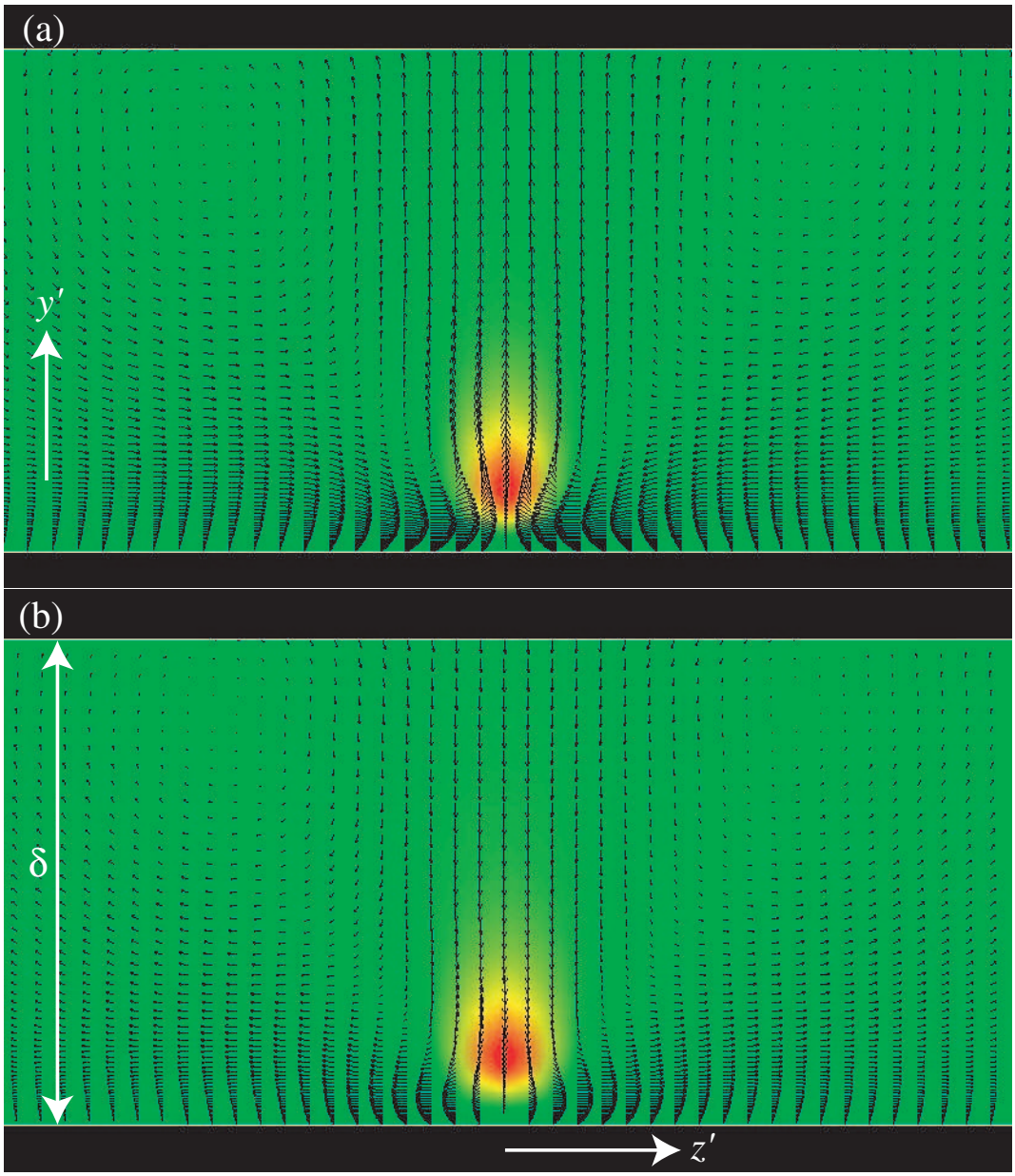

Figure 18: Estimated velocity vector $\hat{u}_r$, $\hat{u}_z$ and Reynolds stress $\hat{u}_\theta \hat{u}_r$ (color) on the concave side. (a) 2nd quadrant; (b) 4th quadrant; $\tau^+ = 0$, $x^+ = 0$.

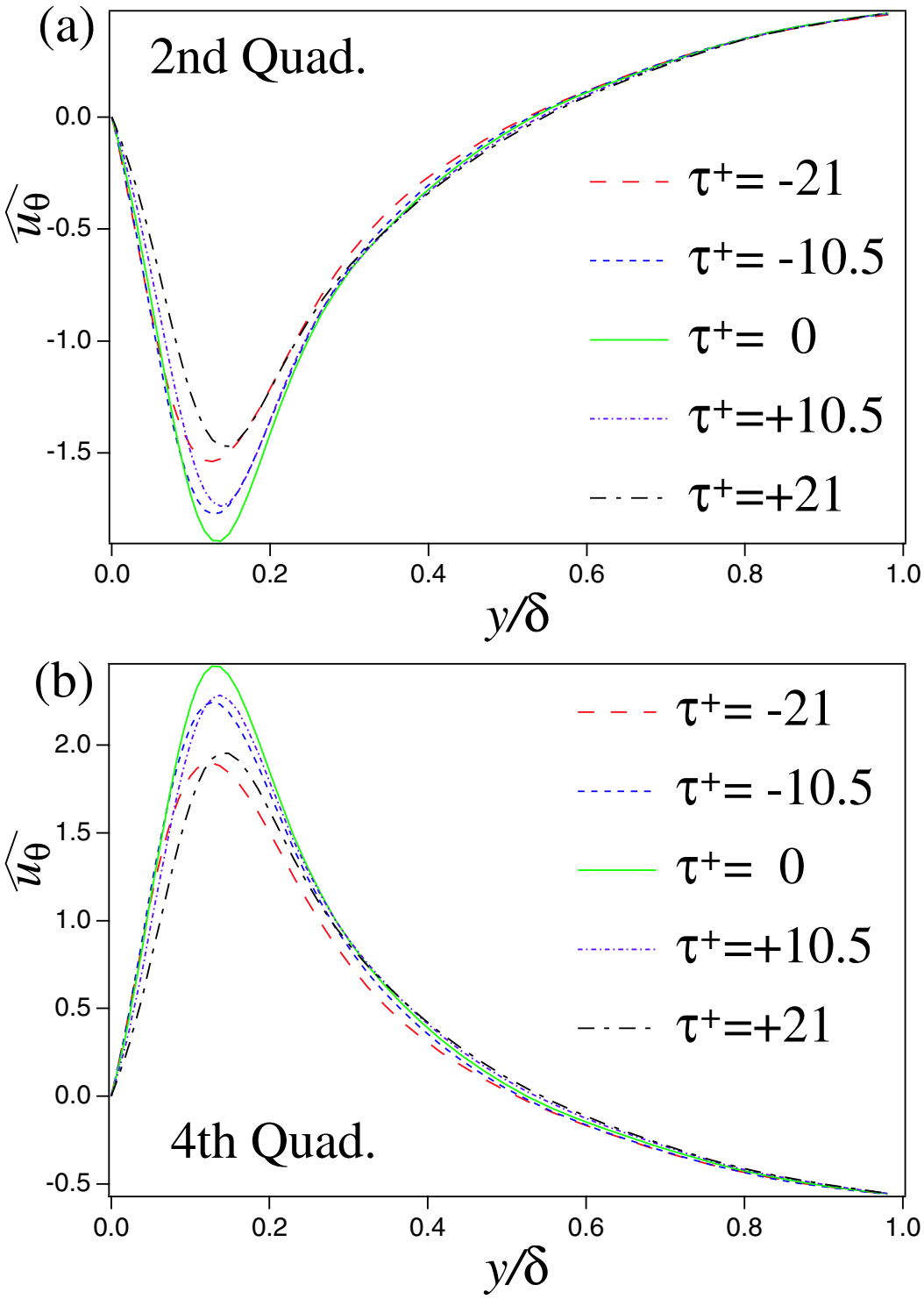

Figure 19: Estimated streamwise velocity on the reference frame moving with convective velocity. Convex side ($x' = 0$ at $\tau = 0$, $z' = 0$). (a) 2nd quadrant; (b) 4th quadrant.

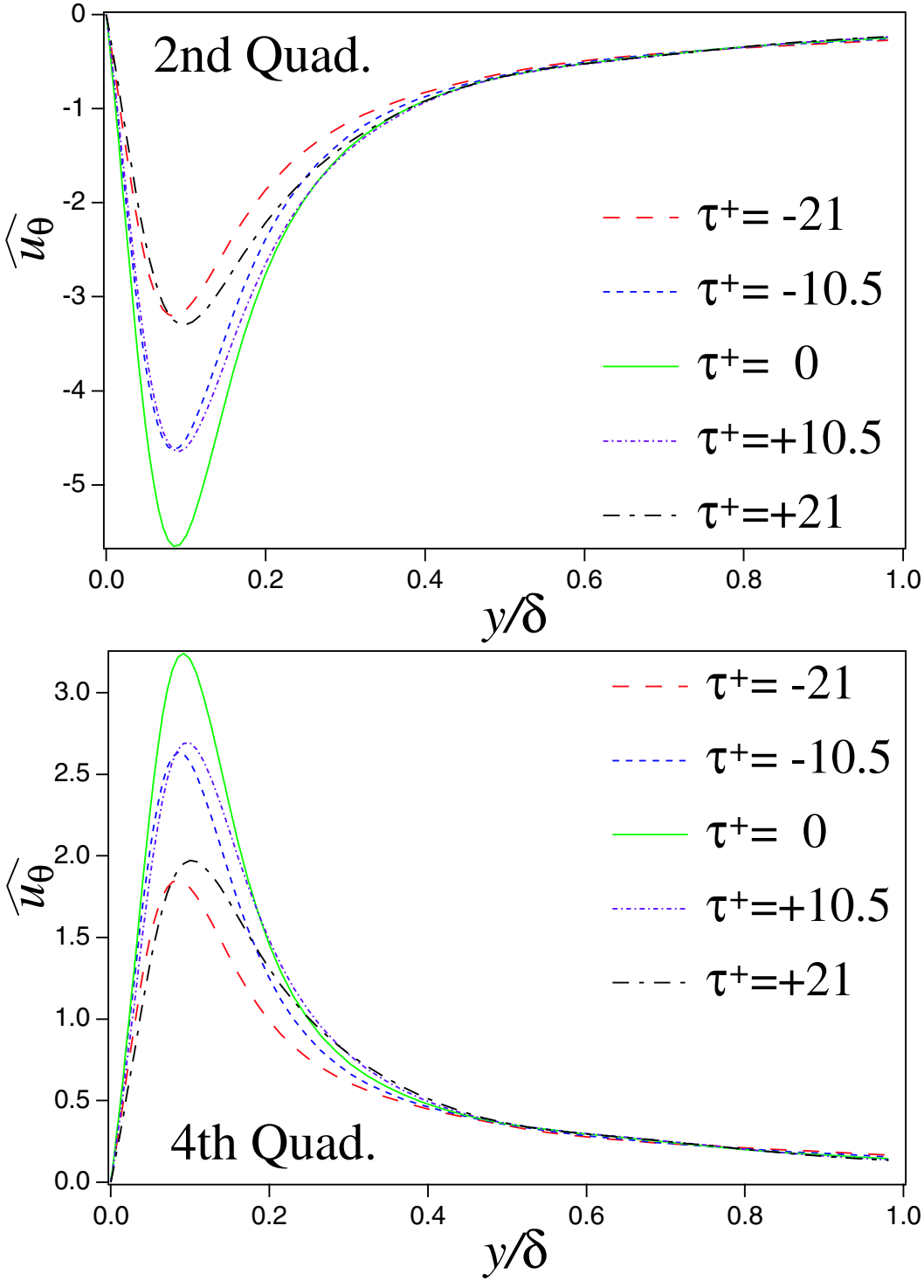

Figure 20: Estimated streamwise velocity on the reference frame moving with convective velocity. Concave side ($x' = 0$ at $\tau = 0$, $z' = 0$). (a) 2nd quadrant; (b) 4th quadrant.

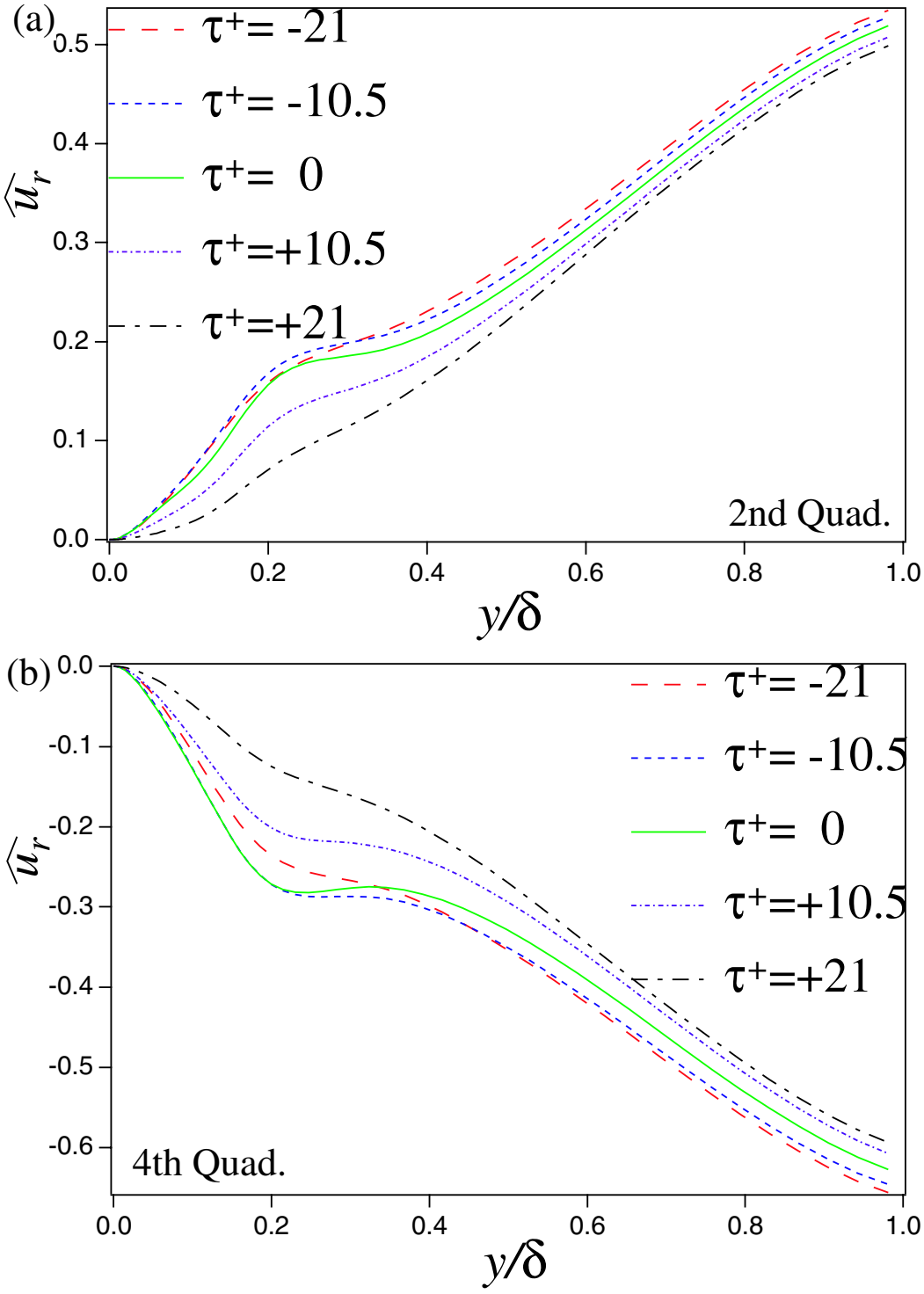

Figure 21: Estimated radial velocity on the reference frame with convective velocity. Convex side ($x' = 0$ at $\tau = 0$, $z' = 0$). (a) 2nd quadrant; (b) 4th quadrant.

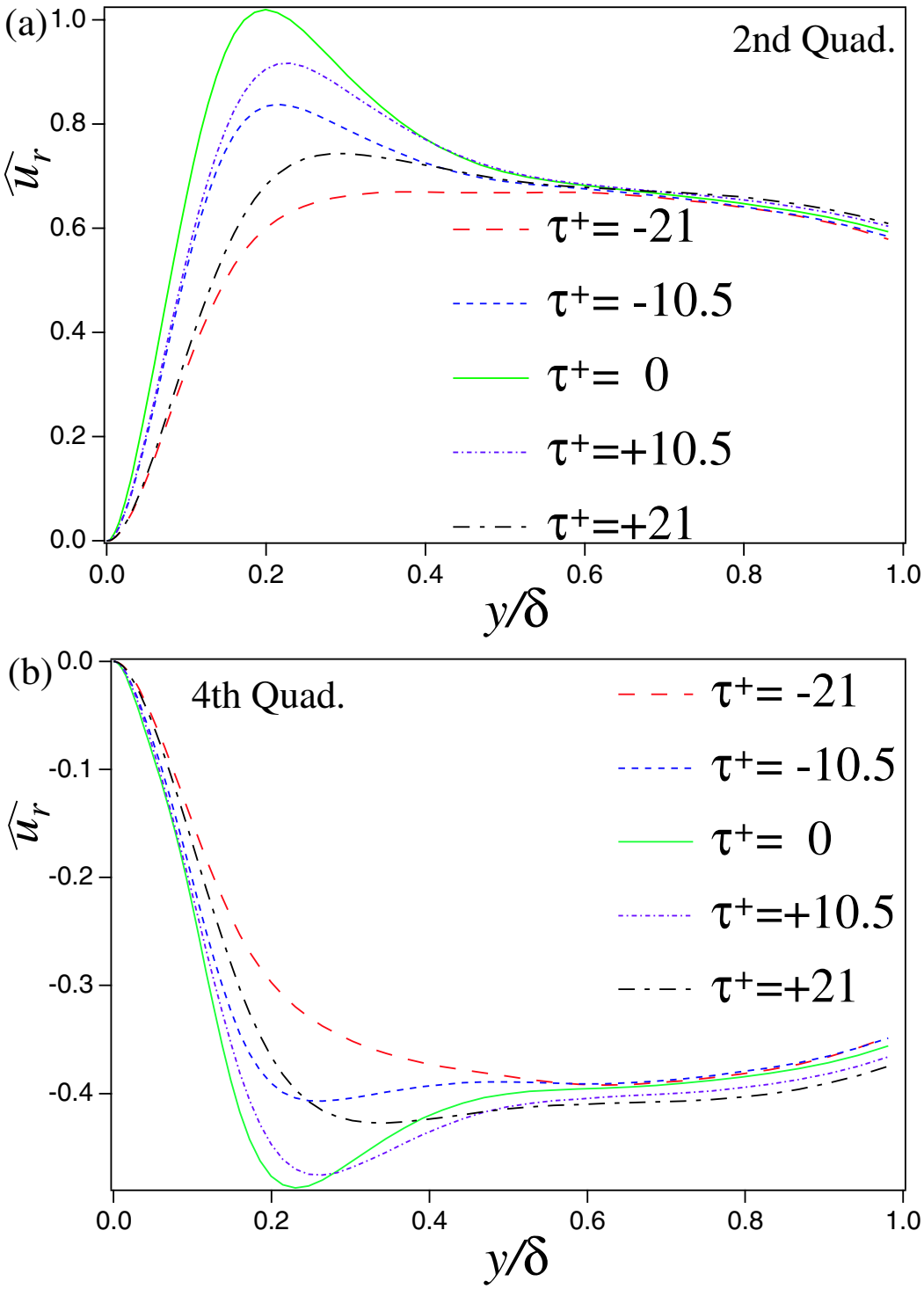

Figure 22: Estimated radial velocity on the reference frame with convective velocity. Concave side ($x' = 0$ at $\tau = 0$, $z' = 0$). (a) 2nd quadrant; (b) 4th quadrant.

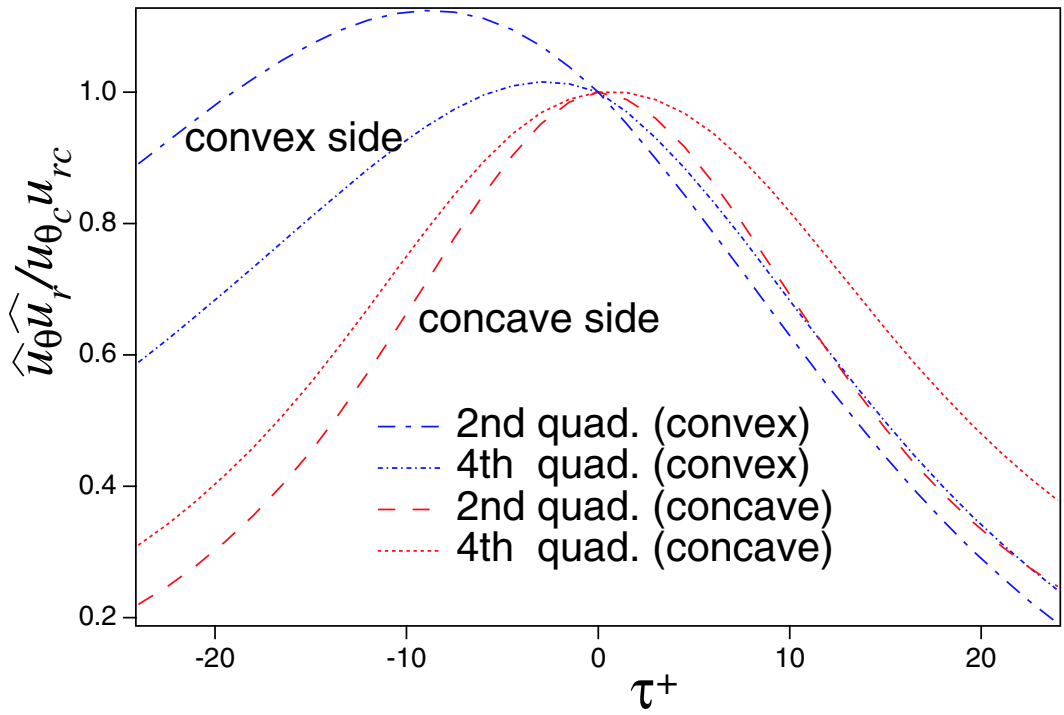

Figure 23: Time dependency of estimated Reynolds shear stress $\hat{u}_\theta \hat{u}_r$ on the reference frame with convective velocity ($x'^+ = 0$ at $\tau^+ = 0$, $y^+ = 15$, $z'^+ = 0$).

Finally, the estimated Reynolds shear stress at $(y^+, z^+) = (15, 0)$ on the convecting reference frame is shown in figure 23 as a function of time. The Reynolds shear stress is normalized by that of the conditional velocities, i.e., $u_{c\theta} u_{cr}$. Significant temporal asymmetry appears on the convex side. Since the estimated streamwise velocity has temporal symmetry, as shown in figure 19, this asymmetry is mainly due to that of the radial velocity (figure 21). On the other hand, developing and decaying processes on the concave side looks nearly symmetric.

Based on the information above, the dynamics of the turbulence-producing eddies, extracted by the spatio-temporal LSE, can be summarized as follows (see, figure 24).

- On the convex side:
  1. Q4 (or Q2) motion is induced by a large-scale roll-cell ($\tau^+ < 0$);
  2. Turbulence producing motion is developed around the velocity condition point ($\tau^+ = 0$);
  3. The motion rapidly decays due to the centrifugal stabilizing effect ($\tau^+ > 0$).
- On the concave side: The centrifugal force works to enhance Q2 and Q4 motions. The development and decay of these motions are autonomic, similarly to plane channel flows.

5 Conclusions

DNS of turbulent curved channel flow is performed to clarify the momentum transport mechanism of turbulent wall shear flow subjected to streamline curvature. According to the turbulence statistics calculated, the following conclusions can be drawn.

1. The radial turbulent intensity is enhanced as the curvature increases. The Richardson number distribution reveals that this trend is due to the extra production by the centrifugal effect.

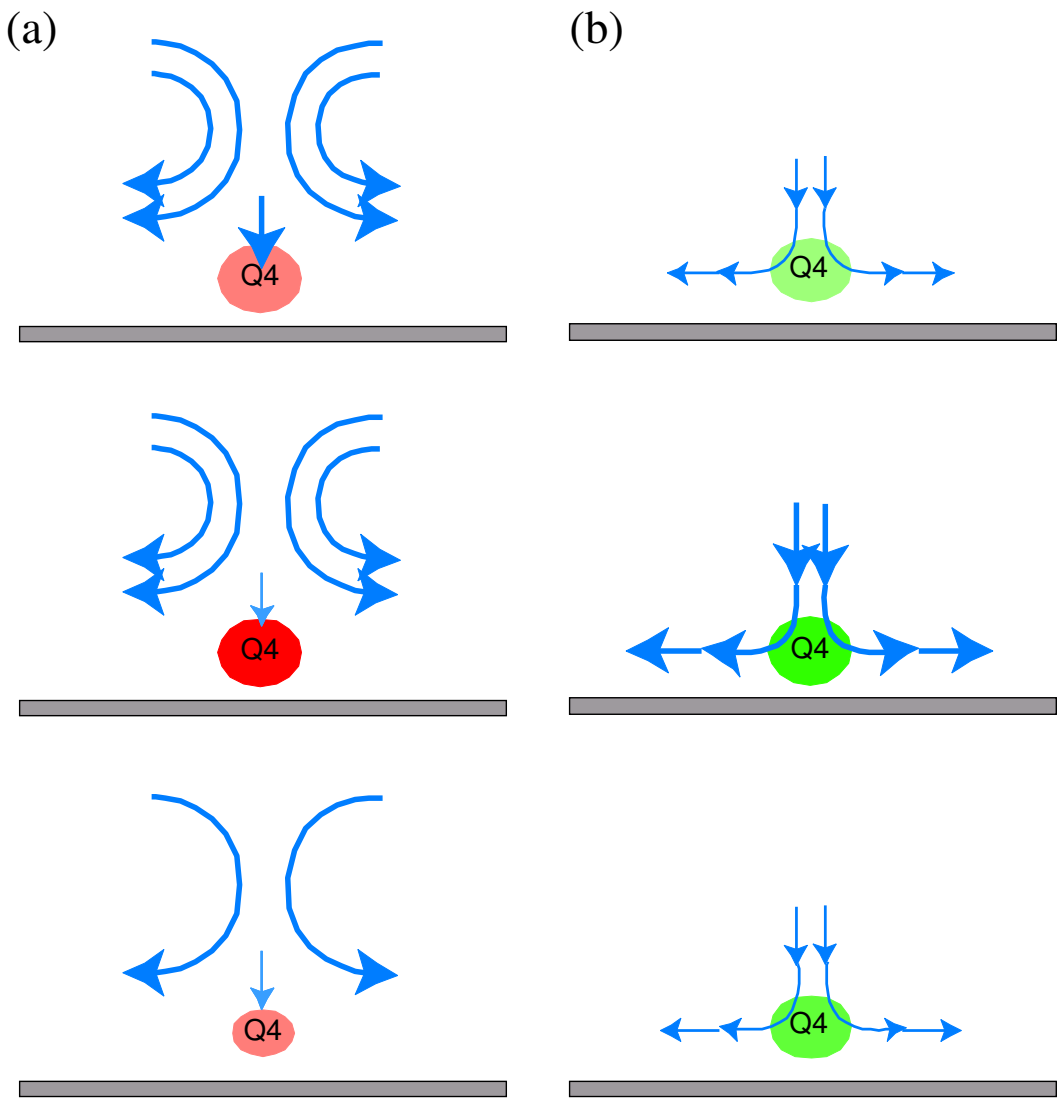

Figure 24: Schematics of the dynamics obtained by the spatio-temporal LSE. (a) Convex side; (b) concave side.

2. On the concave side, there is an inherent mechanism which enhances the turbulent motion. This is clearly illustrated by the distribution of the quadrant contribution to the Reynolds stress.

3. On the convex side, the turbulent motion is suppressed due to the centrifugal stabilizing effect. Although this is qualitatively similar to that is the case of weak curvature [8], the amount of suppression increases as the increase of curvature.

In addition, the spatio-temporal development process of the second- and fourth-quadrant motions is extracted by means of the spatio-temporal linear stochastic estimation, and the following characteristics are found.

1. A large strong roll-cell in the center region of channel works against the centrifugal stabilizing effect on the convex side. The development of turbulent production motion is likely maintained by this roll-cell. On the other hand, roll-cell structure is not observed on the concave side. The turbulence production seems to be self-sustainable.

2. On the convex side, strong outflow and downwash induced by the roll-cell in the center region are confirmed prior to the occurrence of second- and fourth-quadrant motions. On the concave side, a temporal symmetry appears owing to the self sustainable mechanism.

The turbulence statistics computed by the present DNS are available in tabulated forms at the website (http://www.thtlab.t.u-tokyo.ac.jp/).

Acknowledgments

We thank Dr. K. Fukagata for his helpful comments and great efforts to complete this manuscript. This work was supported through the research project on "Micro Gas Turbine/Fuel Cell Hybrid-type Distributed Energy System" by the Department of Core Research for Evolutional Science and Technology (CREST) of the Japan Science and Technology Corporation (JST).

References

[1] Wattendorf F L 1935 A study of the effect of curvature on fully developed turbulent flow *Proc. R. Soc. London* **148** 565-98

[2] Hunt I A and Joubert P N 1979 Effects of small streamline curvature on turbulent duct flow *J. Fluid Mech.* **91** 633–59

[3] So R M C and Mellor G L 1973 Experiment on convex curvature effects in turbulent boundary layers *J. Fluid Mech.* **60** 43–62

[4] Ellis L B and Joubert P N 1974 Turbulent shear flow in a curved duct *J. Fluid Mech.* **62** 65–84

[5] Eskinazi S and Yeh H 1956 An investigation on fully developed turbulent flows in a curved channel *J. Aero. Sci.* **23** 23–34

[6] So R M C and Mellor G L 1975 Experiment on turbulent boundary layers on a concave wall *Aero. Quarterly* **26** 35–40

[7] Gillis J C and Johnston J P 1983 Turbulent boundary-layer flow and structure on a convex wall and its redevelopment on a flat wall *J. Fluid Mech.* **135** 123–53

[8] Moser R D and Moin P 1987 The effects of curvature in wall-bounded turbulent flows *J. Fluid Mech.* **175** 479–510

[9] Choi H, Moin P and Kim J 1993 Direct numerical simulation of turbulent flow over riblets *J. Fluid Mech.* **255** 503–39

[10] Kasagi N, Tomita Y and Kuroda A 1992 Direct numerical simulation of passive scalar field in a turbulent channel flow *Trans. ASME J. Heat Transfer* **114** 598–606

[11] Bradshaw P 1969 The analogy between streamline curvature and buoyancy in turbulent shear flow *J. Fluid Mech.* **36** 177–91

[12] Mansour N N, Kim J and Moin P. 1988 Reynolds-stress and dissipation-rate budgets in a turbulent channel flow *J. Fluid Mech.* **194** 15–44

[13] Wallace J M, Eckelmann H and Brodkey R S 1972 The wall region in turbulent shear flow *J. Fluid Mech.* **54** 39–58

[14] Kim J, Moin P and Moser R 1987 Turbulence statistics in fully developed channel flow at low Reynolds number *J Fluid Mech.* **177** 133–66

[15] Adrian R J 1975 On the Role of Conditional Averages in Turbulent Theory *Turbulence in Liquids* eds Patterspm G and Zakin J (Princeton: Science Press) 322–32

[16] Adrian R J and Moin P 1988 Stochastic estimation of organized turbulent structure: homogeneous shear flow *J. Fluid Mech.* **190** 531–9

[17] Moin P, Adrian R J and Kim J 1987 Stochastic estimation of organized structures in turbulent channel flow *Proc. 6th Turbulent Shear Flow Symp.* Toulouse 16.9.1–8

[18] Zhou J, Adrian R J, Balachandar S and Kendall T M 1999 Mechanisms for generating coherent packets of hairpin vortices in channel flow *J Fluid Mech.* **387** 353–96

[19] Picard C and Delville J 2000 Pressure velocity coupling in a subsonic round jet *Int J Heat Fluid Flow* **21** 359–64

[20] Lumley J L 1967 The structure of inhomogeneous turbulence *Atmospheric turbulence and wave propagation* eds Yaglom A M and Tatarski V I (Moscow: Nauka) 166–78